Paleoceanography and Paleoclimatology

RESEARCH ARTICLE
10.1029/2021PA004267

Special Section:
Cenozoic Evolution of Mountains, Monsoons, and the Biosphere

A ~12 Myr Miocene Record of East Asian Monsoon Variability From the South China Sea

Ann Holbourn[1], Wolfgang Kuhnt[1], Steven C. Clemens[2], and David Heslop[3]

[1]Institute of Geosciences, Christian-Albrechts-University, Kiel, Germany, [2]Earth, Environmental and Planetary Sciences, Brown University, Providence, RI, USA, [3]Research School of Earth Sciences, Australian National University, Canberra, ACT, Australia

Key Points:

- Equable, warm, and humid climate over Southeast Asia during Miocene Climatic Optimum due to latitudinal expansion of tropical convection
- Intensification of seasonal monsoonal regime linked to stepwise climate cooling during middle Miocene Climatic Transition
- Decreased riverine input of alkalinity to ocean due to summer monsoon decline contributed to middle to late Miocene Carbonate Crash

Supporting Information:

Supporting Information may be found in the online version of this article.

Correspondence to:

A. Holbourn,
ann.holbourn@ifg.uni-kiel.de

Citation:

Holbourn, A., Kuhnt, W., Clemens, S. C., & Heslop, D. (2021). A ~12 Myr Miocene record of East Asian Monsoon variability from the South China Sea. *Paleoceanography and Paleoclimatology*, *36*, e2021PA004267. https://doi.org/10.1029/2021PA004267

Received 26 MAR 2021
Accepted 28 MAY 2021

Abstract The long-term evolution of the East Asian Monsoon and the processes controlling its variability under changing climate boundary conditions remain enigmatic. Here, we integrate new and published high-resolution planktic and benthic foraminiferal isotope data with proxy records for chemical weathering derived from diffuse reflectance spectroscopy at Ocean Drilling Program Site 1146 (South China Sea) to reconstruct the evolution of the summer monsoon between ~17 and 5 Ma. Our records show that an overall warm and humid tropical climate prevailed over southeastern Asia during the Miocene Climatic Optimum, suggesting northward expansion of the tropical rain belt in response to greenhouse gas forcing. By contrast, monsoon seasonality increased during the middle Miocene Climatic Transition in tandem with Antarctic glacial expansion and global cooling. Substantial weakening of the summer monsoon between ~12.7 and 10.9 Ma supports that decreased weathering and riverine input of nutrients and alkalinity contributed to carbonate depletion in the deep ocean during the Carbonate Crash. Intensification of monsoonal circulation and strengthening of the biological pump through the late Miocene promoted carbon burial, drawdown of atmospheric CO_2, and climate cooling during the Biogenic Bloom. These results underscore the dynamic evolution of the East Asian Monsoon throughout the middle to late Miocene. Variations in local insolation forcing and in Southern Hemisphere ice volume, influencing the latitudinal thermal gradient, evaporation-moisture budgets, and the strength of the tropical convection, exerted major controls on the development of the monsoon.

1. Introduction

The long-term history of the East Asian Monsoon and the primary controls on its variability remain issues of intense debate. While the seasonal development of the monsoon is intrinsically related to local insolation forcing and the cross-equatorial migration of the Intertropical Convergence Zone (ITCZ), changes in regional topography, in particular the Tibetan-Himalayan orogeny, have long been considered to have exerted a major control on its evolution through the Cenozoic (e.g., An et al., 2001; Kutzbach et al., 1989; Raymo & Ruddiman, 1992). However, the complexities of this vast region's orographic evolution and monsoon dynamics coupled with the ambiguity of monsoon proxy reconstructions have led to widely diverging views concerning the tectonic impact on monsoon circulation (e.g., Biasutti et al., 2018; Kapp & DeCelles, 2019; Spicer et al., 2020).

Recent reviews of the literature support a progressive buildup of the Tibetan Plateau due to early terrane accretion followed by complex deformation and sediment infill linked to the collision of India and Eurasia since the Mesozoic, suggesting that the plateau was already elevated (4–5 km high) by the middle Miocene (Kapp & DeCelles, 2019; Spicer et al., 2020, and references therein). There is also evidence that a relatively rapid uplift of the Himalaya occurred in the latest Oligocene to middle Miocene, leading to a restructuring of wind flow and monsoon precipitation in the early Neogene (Boos & Kuang, 2010; Ding et al., 2017; Spicer et al., 2020). Paleontological and geological data suggested, however, that a monsoonal climate prevailed over southern Asia since the early Paleogene (e.g., Ding et al., 2017; Spicer et al., 2017, 2020) and during the Early Cretaceous (Farnsworth et al., 2019), long before the rise of the Himalaya, implying other driving processes including changes in the interhemispheric thermal gradient, moisture sources, atmospheric circulation, and greenhouse gas concentrations. High-resolution climate simulations additionally indicated that monsoon circulation is largely driven by sea surface temperature gradients and that topography

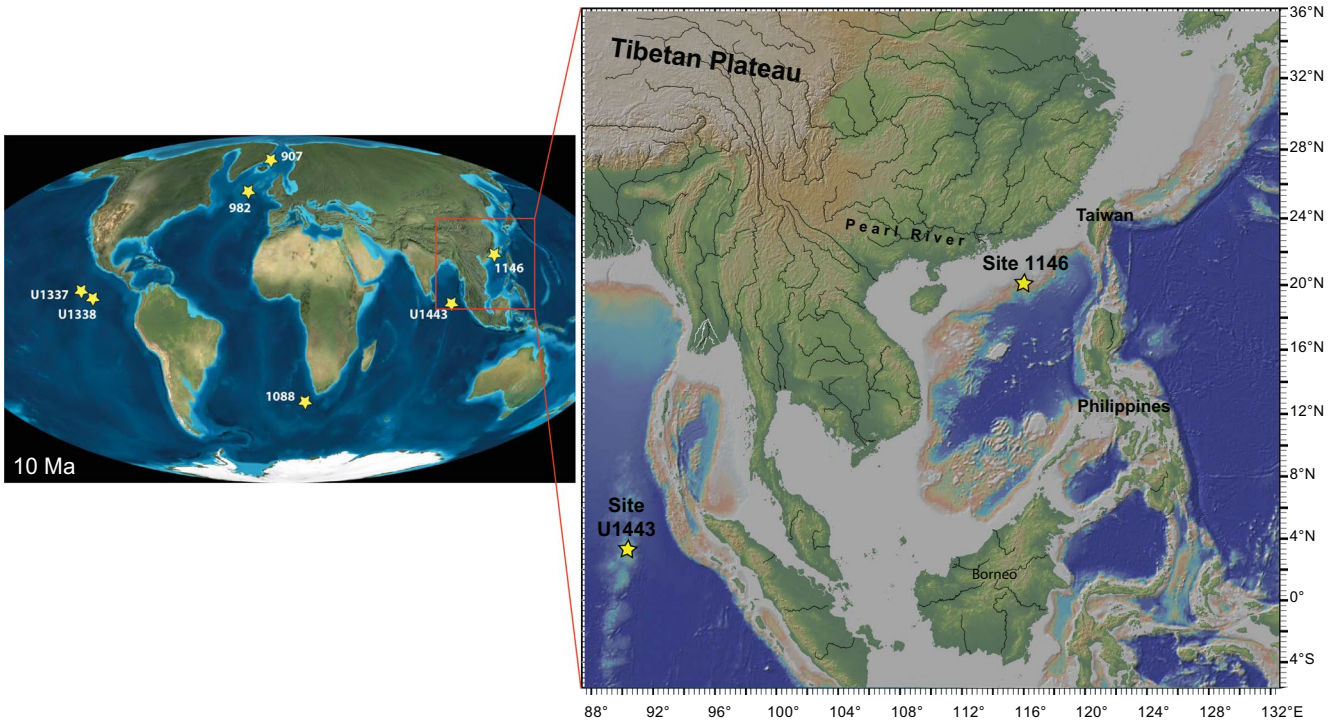

Figure 1. Late Miocene paleogeography (Ron Blakey, Colorado Geosystems) with locations of Ocean Drilling Program (ODP) and International Ocean Discovery Program (IODP) sites referred to in this study. Site 1146 in the northern South China Sea is located offshore Pearl River's drainage basin. Figure made with GeoMapApp (www.geomapapp.org) using the global multi-resolution topography (GMRT) synthesis of Ryan et al. (2009).

mainly redirects monsoon flow and impacts the spatial and temporal distribution of precipitation (Acosta & Huber, 2020).

Reconstructing the past evolution of the East Asian Monsoon during warmer periods of Earth's climate history is especially relevant to better understand the response of this large-scale, highly dynamic climate feature to future climate warming. However, a major handicap to reconstructing the ancient monsoon is the paucity of highly resolved, accurately dated records that can capture the full range of variability and provide insights into the dynamics and forcing mechanisms of the monsoon. Here, we focus on the evolution of the East Asian Monsoon through the middle to late Miocene, an extended interval of global warmth, characterized by the absence of large Northern Hemisphere ice sheets. This period, which postdates the early Neogene phase of Himalayan uplift, encompasses several major transitions associated with stepwise Antarctic ice sheet expansion and global cooling that ushered in fundamentally different regimes of climate variability. We present new planktic foraminiferal isotope data spanning the interval ~12.7–9 Ma from Ocean Drilling Program (ODP) Site 1146 in the northern South China Sea (SCS) (Figure 1), which we integrate with previously published records from the same site (Holbourn et al., 2005, 2007, 2010, 2013, 2018) to derive a continuous, high-resolution (2–4 kyr time step) time series revealing the evolution of near-surface and deep-water masses through the middle to late Miocene. We combine these results with diffuse reflectance spectroscopy (DRS) derived proxy records for chemical weathering at Site 1146 to reconstruct the long-term evolution of the East Asian Monsoon and to investigate relationships between high-latitude and low-latitude climate change between ~17 and 5 Ma.

2. Materials and Methods

2.1. South China Sea ODP Site 1146

ODP Site 1146 (19°N 27.40′N, 116°E 16.37′E, water depth: 2,092 m) is located within a small rift basin on the mid-continental slope in the northern SCS, offshore of the Pearl River (Figure 1; Wang et al., 2000). During the middle to late Miocene, Site 1146 was situated in approximately the same location and water

depth as it is today, and the connection between the SCS and the western Pacific Ocean remained fully open (Hall, 1998; Wang et al., 2000). The location of Site 1146 within the monsoonal rain belt during boreal summer, when the ITCZ migrates into the Northern Hemisphere, is ideal for monitoring long-term changes in monsoonal climate. Today, the region is under the influence of a warm and wet summer monsoon and a cold and dry winter monsoon with the seasonal reversal of monsoonal wind patterns closely linked to the latitudinal swing of the ITCZ. The continuous sediment succession deposited at this site over the late early to late Miocene consists of a relatively homogenous mixture of fine-grained, light brownish gray, hemipelagic carbonate, and clastic sediments (Clift et al., 2014; Wang et al., 2000). The carbonate content within the middle to upper Miocene sequence (Lithological Unit II) varies between 50 and 60 wt% and is in the range of 30–50 wt% in the underlying upper lower to middle Miocene interval (Lithological Unit III) (Wang et al., 2000). The main provenance of the clastic sediment sequence throughout the Miocene was from the vast drainage basin of the Pearl River and its tributaries (Clift et al., 2014; Wang et al., 2000).

2.2. Sampling and Processing

The lower part of the Miocene sediment succession was previously sampled at ~10 cm intervals (~4 kyr mean time resolution), mainly along Hole 1146A (Cores 1146A-61X to 1146A-50X, equivalent to ~17.3–12.8 Ma). The composite middle to upper Miocene sediment sequence spliced from Holes 1146A and 1146C (Cores 1146C-49X to 1146C-30X, equivalent to ~12.8–5 Ma) was sampled at ~5 cm intervals (~2 kyr mean time resolution). Sediment samples were oven dried at 40°C and weighed before washing over a 63 μm sieve. Residues were oven dried at 40°C on a sheet of filter paper, then weighed and sieved into different size fractions.

2.3. Revision of Sediment Splice

Within the upper Miocene interval, we made two adjustments to the shipboard sediment splice (Wang et al., 2000) modified by Holbourn et al. (2007, 2013, 2018). The revised composite depths are referred to as rmcd. (1) We deleted a duplication between 1146C-35X-5, 53 cm (331.43 mbsf) and 1146A-36X-2, 63 cm (330.53 mbsf) corresponding to 350.33 and 352.63 rmcd, which resulted in a deduction of 2.30 m from the splice. (2) We closed a gap between Cores 1146C-37X and 1146A-38X by inserting a 1.45 m segment between 1146A-38X-2, 75 cm (349.95 mbsf corresponding to 372.90 rmcd) and 1146A-38X-3, 70 cm (351.40 mbsf corresponding to 374.35 rmcd) into the splice.

The tie point between the middle to upper Miocene composite section from Holes A and C and the underlying upper lower to middle Miocene sequence, which is mainly from Hole A, is at 1146C-49X-5, 113 cm (460.58 mbsf, equivalent to 495.89 rmcd) and 1146A-50X-2, 37 cm (464.85 mbsf), corresponding to an age of 12.77 Ma. Within the middle Miocene interval, we identified a small sedimentary hiatus in Core 1146A-52X-6, 53 cm (490.03 mbsf), which is visible in the core and core photograph as a slightly oblique unconformity that coincides with a sudden jump of ~0.5 ‰ in the benthic foraminiferal $\delta^{18}O$ and $\delta^{13}C$ records. The identification of this hiatus did not result in any change along the composite depth scale, but was compensated by a short stratigraphic gap in the revised age model.

2.4. Chronology

The chronology of the Miocene sequence at Site 1146 is originally based on correlation of the benthic foraminiferal (mainly *Cibicidoides wuellerstorfi* and/or *Cibicidoides mundulus*) isotope records (Holbourn et al., 2005, 2007, 2013, 2018) to an eccentricity (E) and tilt (T) composite target with an equal weight of eccentricity and obliquity, generated from the La2004 orbital solution (Laskar et al., 2004). We did not include the precession parameter in this composite, as changes between dominant northern (ET−P) or southern (ET+P) hemisphere precessional insolation forcing remain unresolved during the late Miocene. In a few samples (~6%) within the upper lower to middle Miocene interval, other *Cibicidoides* species were analyzed, where *C. wuellerstorfi* and *C. mundulus* were either absent or rare (Holbourn et al., 2005, 2007). Within the interval ~12.8–5 Ma, minor changes were implemented to the original age models of Holbourn et al. (2013, 2018), based on our revision of the sediment splice. Within the interval ~17.3–12.8 Ma, we adjusted the astronomically tuned age model (Holbourn et al., 2005, 2007) to the composite chronology

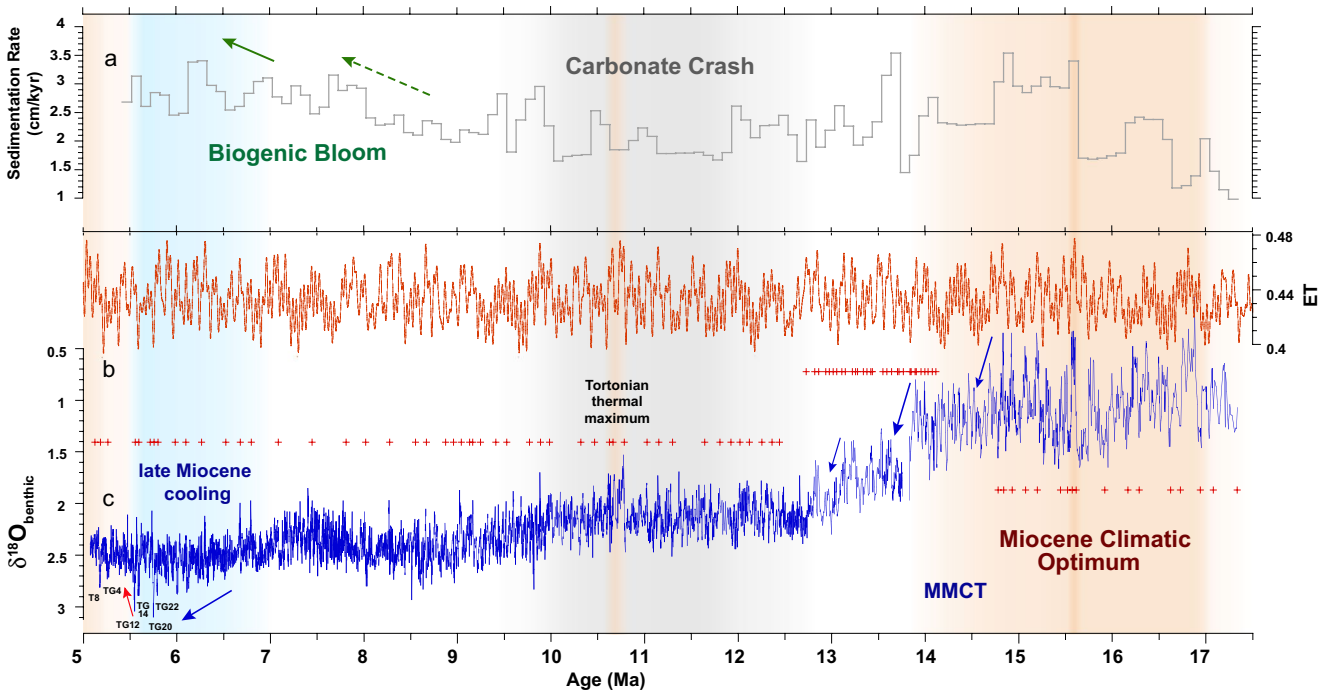

Figure 2. Temporal evolution of benthic foraminiferal $\delta^{18}O$ and sedimentation rates over the interval ~17.3–5 Ma at ODP Site 1146. (a) Sedimentation rates were calculated in 100 kyr bins, based on linear interpolation between age tie points, to compensate for abrupt short-term changes; (b) Eccentricity plus Tilt (ET) tuning target from Laskar et al. (2004); (c) benthic foraminiferal $\delta^{18}O$ from Holbourn et al. (2005, 2007, 2013, 2018) on revised age model. Mean temporal resolution is ~4 kyr between ~17.3 and 12.8 Ma and ~2 kyr between ~12.8 and 5 Ma. Red crosses indicate tuning tie points used to derive age model. Blue arrows indicate main cooling steps. Orange shading indicates intervals of relative global warmth. Blue shading indicates interval of global cooling. Gray shading indicates intense carbonate impoverishment in the deep tropical ocean known as the Carbonate Crash. MMCT: middle Miocene Climatic Transition; Thvera (T) and Thvera-Gilbert (TG) cold stages after Shackleton et al. (1995).

of Integrated Ocean Drilling Program (IODP) Sites U1338 and U1337 (Holbourn et al., 2014, 2015, 2020; Kochhann et al., 2016). The revised depths and ages of the tie points used to derive the chronology at Site 1146 are provided in Table S1 and are shown in Figure 2. The stable isotope data with revised depths and ages are available at https://doi.org/10.1594/PANGAEA.931111.

2.5. Planktic Foraminiferal Isotopes

For this study, new planktic foraminiferal stable isotope data (>1,600 samples) were generated at ~5 cm intervals over the composite sequence spanning the interval ~12.7–9 Ma at Site 1146. Approximately 20 specimens of the mixed-layer dweller *Trilobatus sacculifer* were picked from the 250 to 315 μm size fraction for $\delta^{18}O$ and $\delta^{13}C$ analysis. Samples were sonicated in ethanol to remove fine clays, homogenized, and subsampled (~80 μg $CaCO_3$) for analysis on the Brown University MAT252 IRMS coupled to a Kiel III carbonate device. Samples were reacted by individual acid addition (99% H_3PO_4 at 70°C). Repeated analyses of Brown Yule Marble ($n = 116$, 1σ) yields -2.27 ± 0.03 for $\delta^{13}C$ and -6.48 ± 0.07 for $\delta^{18}O$. Carrara Marble ($n = 198$, 1σ) yield 2.03 ± 0.03 for $\delta^{13}C$ and -1.89 ± 0.05 for $\delta^{18}O$. Statistics on replicate analysis of homogenized samples are indistinguishable from those of the standards. All results were calibrated to the National Institute of Standards and Technology (Gaithersburg, MD) carbonate isotope standard NBS 19 and are reported as ‰ VPDB.

These new measurements complement previously published planktic foraminiferal isotope records spanning the intervals ~15.7–12.8 Ma (Holbourn et al., 2010) and ~9–5 Ma (Holbourn et al., 2018). The near-surface, mixed-layer species *Globigerinoides obliquus* or *Globigerinoides subquadratus* (size fraction 250–350 μm) were measured over the interval ~15.7–12.8 Ma. Paired measurements in 51 samples indicated no significant offset in $\delta^{18}O$ and $\delta^{13}C$ between these two species (Holbourn et al., 2010). Over the interval ~9–5 Ma, *T. sacculifer* (size fraction 250–315 μm) was analyzed (Holbourn et al., 2018). The published data

sets over the intervals ~15.7–12.8 Ma and ~9–5 Ma were integrated with our new records to provide continuous, high-resolution isotope time series between ~17.3 and 5 Ma. All data are plotted and reported relative to *T. sacculifer*. The *G. obliquus/G. subquadratus* isotope values were adjusted to those of *T. sacculifer* by adding 0.23‰ to $\delta^{13}C$ and 0.43‰ to $\delta^{18}O$. The stable isotope data with revised depths and ages are available at https://doi.org/10.1594/PANGAEA.931111.

2.6. Time Series Analysis

Stratigraphic correlation of depth and time series, evenly spaced linear interpolation, detrending, and filtering were performed with AnalySeries 2.0.8 (Paillard et al., 1996). Coherence and phase of planktic and benthic $\delta^{18}O$ and $\delta^{13}C$ time series were estimated with Blackman-Tukey cross-spectral analysis using a Bartlett window. Spectral analyses on unevenly spaced time series with the REDFIT function of Schulz and Mudelsee (2002) were performed with Past4.04 (Hammer et al., 2001), using a Blackman-Harris window of two segments, a frequency oversampling value of 2 and Monte Carlo simulation of confidence intervals based on parametric approximation (chi-square test). We divided the time series into four distinct intervals for analysis, based on changes in cyclicity and signal amplitude identified in the evolutive spectra at ~7, 9, and 10.8 Ma. For evolutive spectra, we used the wavelet transform function in Past4.04, which is based on the algorithm of Torrence and Compo (1998), on an evenly spaced time series with 1 kyr resolution. We used a Morlet wavelet, $p = 0.05$ significance level calculation from a chi-square test and displayed the cone of influence that demarks the area affected by boundary effects.

2.7. Visible Light Spectroscopy Proxies of Continental Weathering and Erosion

During ODP Leg 184, shipboard DRS was performed with a Minolta CM-2002 instrument, using a wavelength resolution of 10 nm across the wavelength spectrum of visible light (400–700 nm). Measurements were taken immediately after retrieval of the cores at intervals of 5 cm following calibration to black and white standards (Wang et al., 2000). DRS has been successfully used to evaluate changes in the mineralogical composition of fine-grained marine sediments and to quantify the distribution of iron oxides and oxyhydroxides such as hematite and goethite, clay minerals, carbonate, and organic matter (Balsam & Damuth, 2000; Balsam et al., 2007; Clift et al., 2008, 2014; Deaton & Balsam, 1991; Debret et al., 2011). In particular, hematite and goethite strongly influence the color spectra of bulk sediment and can be detected at extremely low concentrations (Giosan et al., 2002; Harris & Mix, 1999, 2002; Zhang et al., 2007). Intensely red hematite is a characteristic iron oxide of arid areas, while the yellowish oxyhydroxide goethite is formed in soils under more humid conditions (Kämpf & Schwertmann, 1983; Schwertmann, 1971).

In this study, we used the ratio of percent diffuse reflection in the 560 and 430 nm bands as a proxy for the abundance of hematite relative to goethite (Figures S1–S3), following Deaton and Balsam (1991) and Harris and Mix (1999, 2002). This approach is applicable over the entire record between ~17 and 5 Ma, while endmember-based unmixing of the DRS data could only be used over the interval between ~15.6 and 10.8 Ma, which is not affected by episodes of secondary diagenetic alteration under oxygen-deficient sedimentary conditions (Figure S3). For this shorter interval, we used endmember-based unmixing following the method outlined in Heslop et al. (2007). We additionally calculated C_{RAT}, which is defined as the mineralogical ratio of the greenish clay mineral chlorite and the sum of chlorite, hematite, and goethite and has been used as an indicator of continental weathering and erosion (Clift et al., 2008). Details of this method are provided in the Supporting Information and the data are available at https://doi.org/10.1594/PANGAEA.931111.

3. Results

3.1. Chronology

The Site 1146 chronology over the interval 12.8–5 Ma is based on minimal tuning of the benthic foraminiferal $\delta^{18}O$ record to the orbital solution of Laskar et al. (2004), using 48 age tie points along the revised sediment splice between Holes 1146A and 1146C (Table S1 and Figure 2). Modifications of the splice led to minor revisions of the age models in Holbourn et al. (2018) and De Vleeschouwer et al. (2020), which were both based on the splice version published in Holbourn et al. (2018). Revision of the chronology

between ~17.3 and 12.7 Ma, based on correlation to the benthic foraminiferal isotope record of Site 1146 to the composite records of Integrated Ocean Drilling Program (IODP) Sites U1338 and U1337 in the eastern equatorial Pacific Ocean (Holbourn et al., 2014, 2015, 2020; Kochhann et al., 2016), resulted in minor adjustments between ~15.8 and 12.7 Ma. However, the revised age model before ~15.8 Ma indicates a substantial extension of the stratigraphic interval represented at Site 1146. Based on the revised age model, the Miocene sedimentary succession at Site 1146 has a basal age of ~17.3 Ma. The mean sedimentation rate is ~2.5 cm kyr^{-1} with a maximum of 3.5 cm kyr^{-1} and a minimum of 1 cm kyr^{-1} over the interval 17.3–5 Ma (Figure 2). Sedimentation rates notably show a marked decrease before ~16.6 Ma.

The benthic foraminiferal $\delta^{18}O$ series predominantly exhibits 41 kyr variability over the intervals ~14.7–14.2, ~12.7–12.2, ~9.7–9.2, and ~7.7–7.2 Ma, reflecting the high-amplitude of obliquity variations and the low-amplitude of the short eccentricity (100 kyr) cycle during these periods (Figure 3). The onset of the MCO at ~16.9 Ma corresponds to a sharp decrease in benthic foraminiferal $\delta^{18}O$ at high eccentricity, which correlates to similar negative $\delta^{18}O$ excursions in the Pacific Ocean (Integrated Ocean Drilling Program (IODP) Site U1337; Holbourn et al., 2015) and the Indian Ocean (International Ocean Discovery Program [IODP] Site U1443; Lübbers et al., 2019). Further important correlative $\delta^{18}O$ markers are the "hyperthermal" minimum at 15.6 Ma, the major increase between 13.91 and 13.84 Ma, associated with the main expansion of the East Antarctic Ice sheet (Holbourn et al., 2005), and the last prominent "hyperthermal" minimum at 10.8 Ma ("Tortonian thermal maximum" of Westerhold et al. [2020]). In addition, the interval 6–5 Ma includes several prominent transient $\delta^{18}O$ maxima, identified as Thvera (T) and Thvera-Gilbert (TG) cold stages T8, TG4, TG12, TG14 TG20, and TG22 (Shackleton et al., 1995; Shackleton & Hall, 1997), which provide excellent stratigraphic control in the uppermost part of the record (Figure 2). Higher frequency (100 kyr eccentricity and 41 kyr obliquity) variability of benthic and planktic foraminiferal $\delta^{13}C$ is superimposed upon low-frequency oscillations that broadly relate to the ~400 kyr long eccentricity cycle (Figure 3). Comparison of the benthic and planktic foraminiferal $\delta^{18}O$ and $\delta^{13}C$ records, plotted in the depth and time domains, shows that the original spectral characteristics are preserved following the tuning procedure.

3.2. Planktic Foraminiferal Isotopes

During the end phase of the MCO (~15.7–14.7 Ma), *G. obliquus/G. subquadratus* mean $\delta^{18}O$ oscillates between −1.9‰ and −2.7‰ and exhibits relatively high amplitude variability (stdev mainly between 0.35‰ and 0.1‰) (Figures 3 and S4–S5). Mean $\delta^{18}O$ decreases to −2.8 after 14.7 Ma, then shows a major stepwise increase to −1.8, which is matched by a stepwise decrease in amplitude variability from 0.45‰ to 0.1‰, over the interval 14.7–13.5 Ma that includes the MMCT (14.7–13.8 Ma) and the last $\delta^{13}C$ maximum of the Monterey Excursion (CM6). From 13.5 to 12.8 Ma, mean $\delta^{18}O$ remains between −1.6‰ and −2.1‰ with amplitude variability between 0.25‰ and 0.05‰. After ~12.7 Ma, *G. sacculifer* mean $\delta^{18}O$ fluctuates between −1.8‰ and −2.1‰ and displays extremely low amplitude variability (stdev below 0.15‰) until ~ 11.6 Ma (Figures 3, 4, and S4–S5). A stepwise decrease in mean $\delta^{18}O$ from −1.8‰ to −2.4‰ is coupled to a slight increase in amplitude variability (stdv: 0.25‰–0.05‰) between ~11.6 and 10.9 Ma. This is followed by a steep rise to −1.6‰ at ~10.8 Ma during the Tortonian thermal maximum, which corresponds to a major decrease in benthic foraminiferal $\delta^{18}O$ (Figures 3, 4, and S4–S5). Mean $\delta^{18}O$ decreases sharply to −2.6‰ following the Tortonian thermal maximum, then displays an increasing trend, reaching −1.9‰ at 9.4 Ma (stdv: 0.25‰–0.05‰). From 9.4 to 7 Ma, mean values oscillate between −1.9‰ and −2.2‰, (stdv mainly < 0.2‰), exhibiting a slightly increasing trend between ~7.7 and 7 Ma (Figures 3 and S4–S5). At ~7 Ma, mean $\delta^{18}O$ shows a marked increase of ~0.3‰, then values vary between −1.9‰ and −1.4‰ and display higher amplitude variability (stdev mainly between 0.1‰ and 0.25‰) until ~5.5 Ma. After a marked decrease to −2.0‰ at 5.5 Ma, mean values remain relatively low until 5 Ma.

Benthic and planktic foraminiferal $\delta^{13}C$ exhibit relatively consistent long-term (~400 kyr) and shorter-term (~100 and ~41 kyr) variability between ~16 and 5 Ma (Figure 3). A salient feature of the $\delta^{13}C$ curves is the prominent positive carbon-isotope excursion, known as the Monterey Excursion (Vincent & Berger, 1985; Woodruff & Savin, 1991), which exhibits a pronounced ~400 kyr rhythm between ~16.7 and 13.5 Ma (Holbourn et al., 2007). After ~13.5 Ma, mixed layer mean $\delta^{13}C$ decreases markedly (from ~2.8‰ to 2‰) and displays low-frequency oscillations (stdev mainly between ~0.05‰ and 0.2 ‰) until ~9 Ma (Figures 3, 4, and S4–S5). This long-term trend is interrupted by a sharp, transient negative shift centered at 10.8 Ma

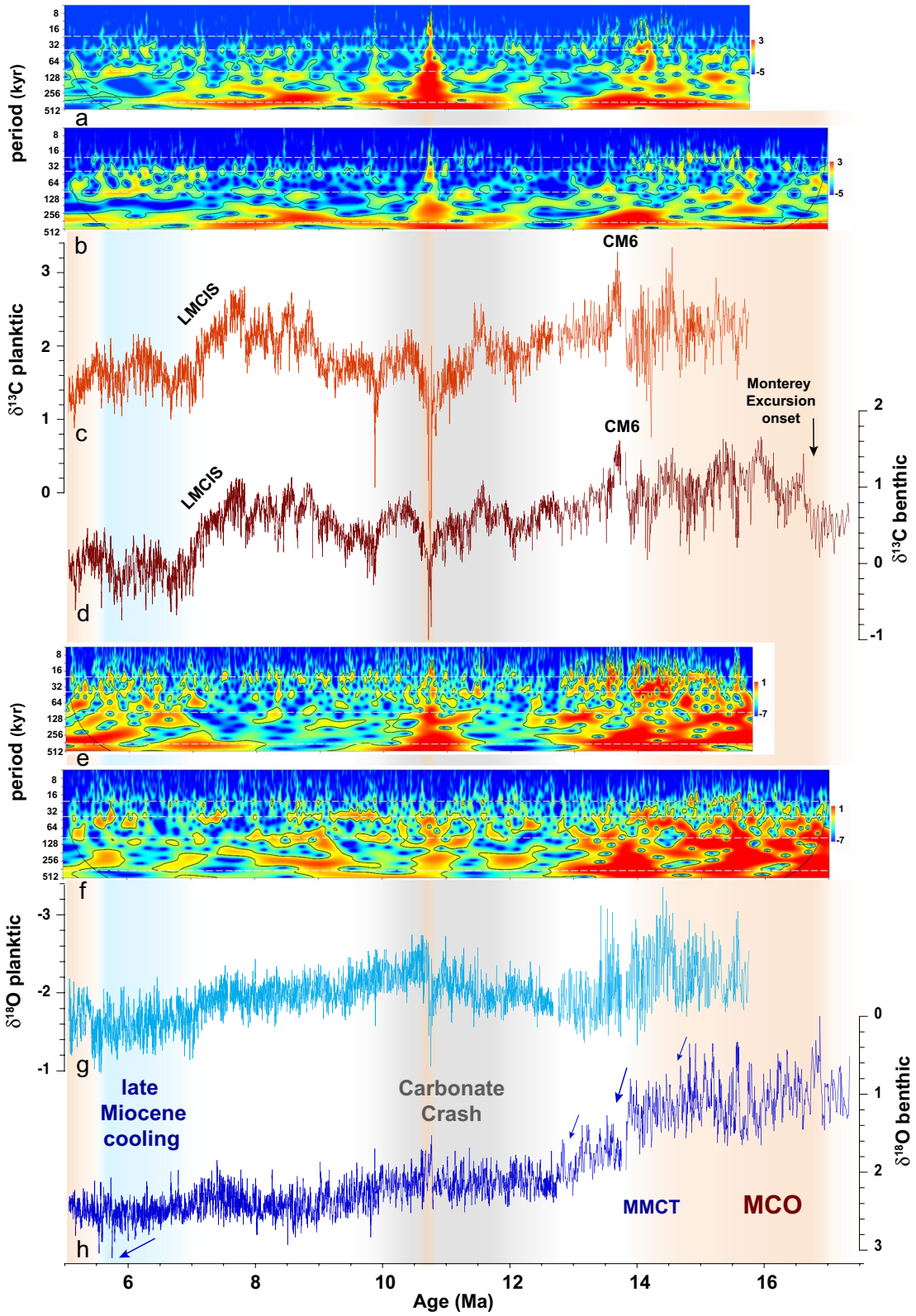
period (kyr)
a
b
CM6
LMCIS
δ13C planktic
c
CM6
Monterey
Excursion
onset
LMCIS
d
δ13C benthic
period (kyr)
e
f
δ18O planktic
g
late
Miocene
cooling
Carbonate
Crash
MMCT
MCO
h
δ18O benthic
Age (Ma)

Figure 3

during the Tortonian thermal maximum. From ~9 to 7.7 Ma, mixed layer $\delta^{13}C$ shows a distinct increase (mean oscillates between 1.8‰ and 2.6‰; stdev mainly between 0.1‰ and 0.4‰). Between ~7.7 and 7 Ma, mixed layer $\delta^{13}C$ is characterized by a long-term decrease from ~2.7‰ to 1.3‰, which corresponds to the global $\delta^{13}C$ decline, known as the Late Miocene Carbon Isotope Shift (LMCIS). Following the LMCIS, mean $\delta^{13}C$ fluctuates between 1.2‰ and 1.8‰ and displays higher amplitude variability (stdev generally between 0.1‰ and 0.6‰). The gradient between planktic and benthic foraminiferal $\delta^{13}C$ ($\Delta\delta^{13}C$), which provides a measure of the strength of the global ocean's biological pump (Hain et al., 2014), shows an overall decline from 1.6 to 1.1 between ~13 and 10 Ma, followed by a long-term increase after ~9 Ma, reaching maximum values of 1.9 at ~6 Ma (Figures 5 and S6).

3.3. Temporal Evolution of Chemical Weathering Proxy: Hematite/Goethite

Between ~17 and 5 Ma, hematite/goethite, a chemical weathering proxy for aridity, exhibits distinct trends that characterize different phases of climate evolution (Figure 5). During the MCO, hematite/goethite displays relatively low amplitude variability as well as the lowest mean values (~1.1) within the entire record. In the early part of the MMCT, hematite/goethite shows a stepwise increase, reaching ~1.35 at ~13.8 Ma, then fluctuates between 1.15 and 1.3 until ~12.7 Ma. A steep increase to ~1.5 after 12.7 Ma marks the onset of an interval with the highest values within the entire record, corresponding to an extended period of aridity that lasted until ~10.9 Ma. This interval is also characterized by higher amplitude oscillations between ~1.2 and ~1.5, indicating a more variable climate regime.

In the interval 15.6–10.8 Ma, not affected by episodic diagenetic alteration of iron oxides/oxyhydroxides, endmember analysis of the reflectance spectra at Site 1146 enabled discrimination of a goethite + hematite end member (EM1) and a chlorite endmember (EM3), which were used to calculate the physical erosion proxy C_{RAT} (Figure S3). The EM1 record exhibits similar long-term trends as hematite/goethite. The MCO interval 15.6–14.7 Ma is characterized by low amplitude variability and extremely low mean values (0–0.1), whereas during the early part of the MMCT (14.7–13.8 Ma) amplitude variability is high (between 0 and 0.3) and EM1 displays an overall increasing trend. This is followed by a plateau with a long-term mean of ~0.3 until ~12.7 Ma. A marked increase after ~12.7 Ma marks the onset of an interval with sustained high values, which fluctuate between 0.25 and 0.45 until ~10.9 Ma.

Between ~10.9 and 9 Ma, hematite/goethite exhibits a decrease from ~1.5 to 1.2, which is punctuated by three intervals of unusually low values (~1.1), centered at 10.8, 9.8, and 9.0 Ma (Figures 4 and 5). The sediment within these intervals displays a greenish-gray color and contains pyrite, indicating an early diagenetic reduction of iron oxides due to dysoxic conditions during sedimentation. This episodic diagenetic alteration prohibits the estimation of weathering conditions in the terrigenous source area, based on hematite/goethite. From ~9 to 7 Ma, hematite/goethite shows relatively low amplitude variability with mean values between 1.2 and 1.3, except for a transient interval of dysoxic conditions at ~7 Ma (Figure 5). Between ~7 and 5.5 Ma, mean values increase, varying between 1.35 and 1.25, then shift to slightly lower values between 1.25 and 1.2 after 5.5 Ma.

3.4. Time Series Analysis

The Morlet wavelet power spectrum of planktic foraminiferal $\delta^{18}O$ over the interval 17–5 Ma indicates the highest power at the precessional band and at the short and long eccentricity bands between ~15.6 and 13.8 Ma (Figure 3). However, the near-surface dwelling *G. obliquus* and *G. subquadratus* were analyzed

Figure 3. Response of foraminiferal $\delta^{18}O$ and $\delta^{13}C$ from ODP Site 1146 to orbital forcing between ~17.3 and 5 Ma. (a) Wavelet power spectrum of mixed layer $\delta^{13}C$; (b) wavelet power spectrum of benthic foraminiferal $\delta^{13}C$; (c) mixed layer $\delta^{13}C$; new data between 12.7 and 9 Ma were integrated with previously published data (Holbourn et al., 2010, 2018); (d) benthic foraminiferal $\delta^{13}C$ from Holbourn et al. (2005, 2007, 2013, 2018); (e) wavelet power spectrum of mixed layer $\delta^{18}O$; (f) wavelet power spectrum of benthic foraminiferal $\delta^{18}O$; (g) mixed layer $\delta^{18}O$; new data between 12.7 and 9 Ma were integrated with previously published data (Holbourn et al., 2010, 2018); (h) benthic foraminiferal $\delta^{18}O$ from Holbourn et al. (2005, 2007, 2013, 2018). All data are plotted on revised age model. Blue arrows indicate main cooling steps. Orange shading indicates intervals of relative global warmth. Blue shading indicates interval of global cooling. Gray shading indicates intense carbonate impoverishment in the deep tropical ocean known as the Carbonate Crash. MCO: Miocene Climatic Optimum; MMCT: middle Miocene Climatic Transition; CM6: last $\delta^{13}C$ maximum within Monterey Excursion; LMCIS: Late Miocene Carbon Isotope Shift. White dashed lines mark 23, 41,100, and 400 kyr orbital bands.

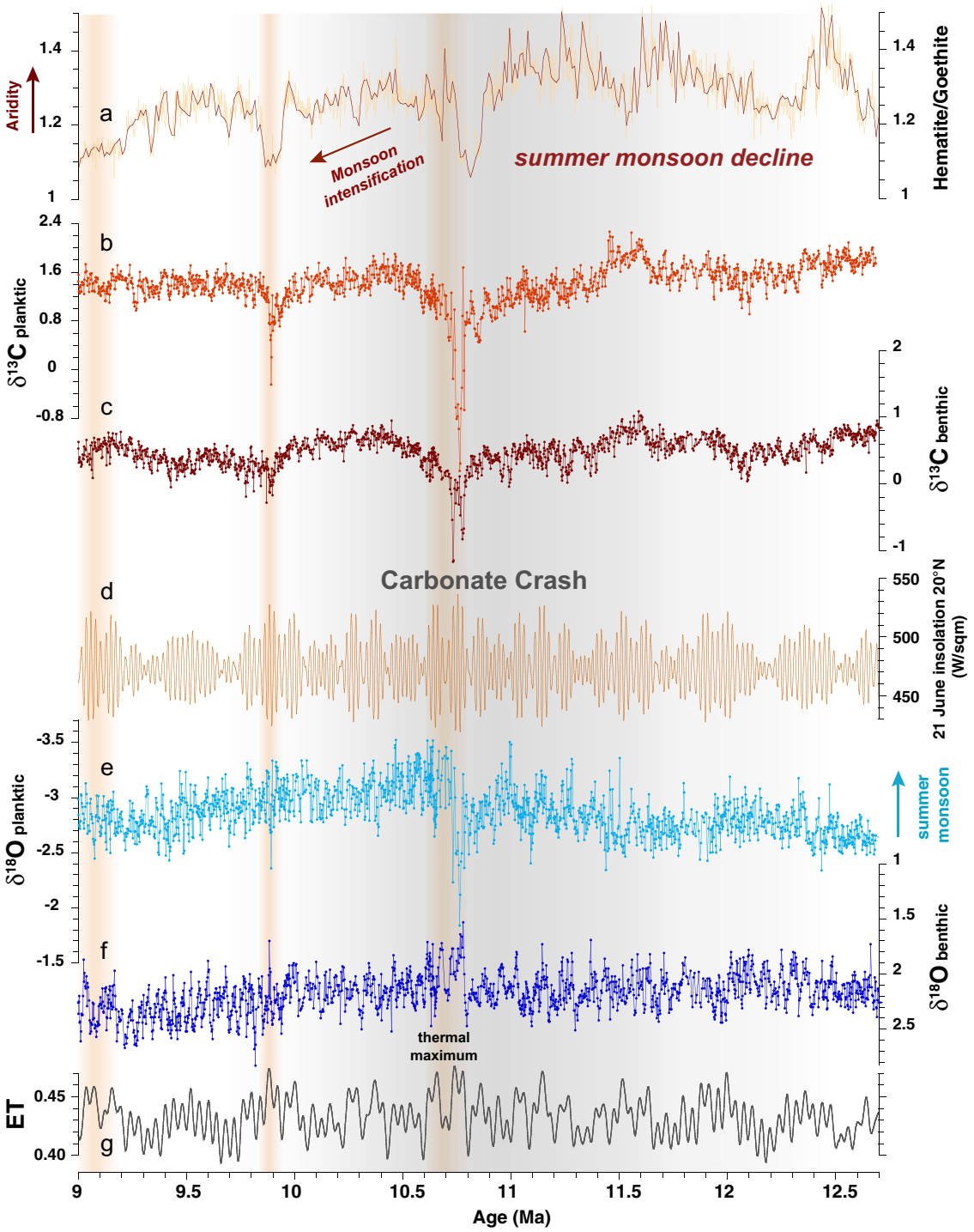

Figure 4. Expanded view of interval 12.7–8.7 Ma at ODP Site 1146. (a) DRS-derived chemical weathering proxy record; dark brown smoothed curve based on Stineman function; (b) new mixed layer $\delta^{13}C$; (c) benthic foraminiferal $\delta^{13}C$ from Holbourn et al. (2013, 2018); (d) 21st June insolation at 20°N from Laskar et al. (2004); (e) new mixed layer $\delta^{18}O$; (f) benthic foraminiferal $\delta^{18}O$ from Holbourn et al. (2013, 2018). All data are plotted on revised age model; (g) Eccentricity plus Tilt (ET) from Laskar et al. (2004). Orange shading indicates intervals of relative global warmth coincident with episodes of decreased bottom water ventilation. Gray shading indicates intense carbonate impoverishment in the deep tropical ocean known as the Carbonate Crash.

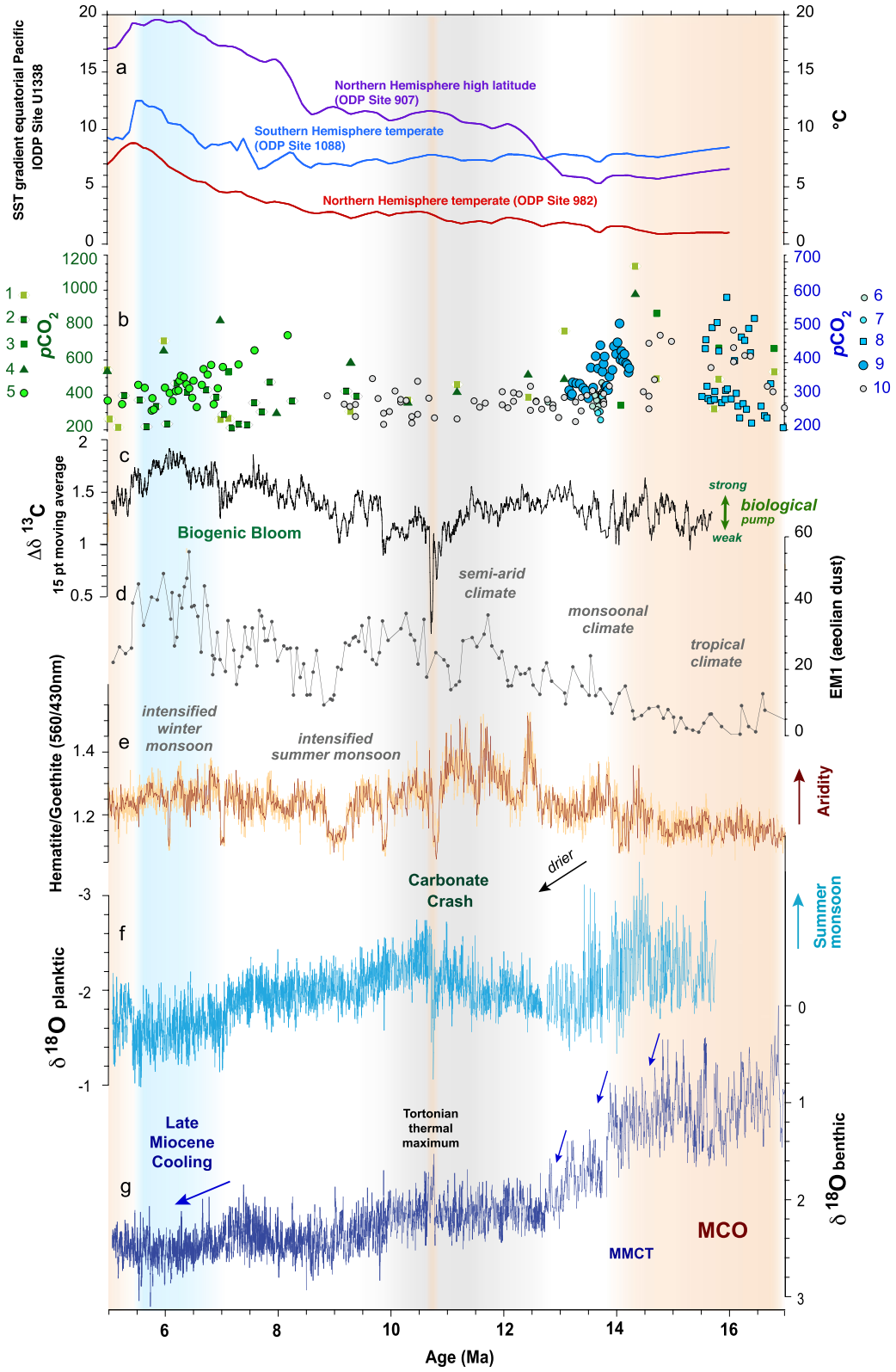
SST gradient equatorial Pacific IODP Site U1338
a
Northern Hemisphere high latitude (ODP Site 907)
Southern Hemisphere temperate (ODP Site 1088)
Northern Hemisphere temperate (ODP Site 982)
°C
b
pCO2
c
Δδ13C 15 pt moving average
Biogenic Bloom
strong
biological pump
weak
d
semi-arid climate
monsoonal climate
tropical climate
EM1 (aeolian dust)
e
Hematite/Goethite (560/430nm)
intensified winter monsoon
intensified summer monsoon
Aridity
drier
Carbonate Crash
f
δ18O planktic
Summer monsoon
Late Miocene Cooling
Tortonian thermal maximum
g
MCO
MMCT
δ18O benthic
Age (Ma)

Figure 5

within this interval, which may result in higher amplitude variability than for the slightly deeper the mixed layer dweller *T. sacculifer*. Within the interval ~14.7–14.1 Ma, we additionally note high spectral power in the obliquity band, when obliquity forcing is dominant and short eccentricity shows low amplitude variability (Figure 3).

Spectral analysis of the *T. sacculifer* $\delta^{18}O$ record over individual time slices within the interval 12.7–5.0 Ma reveals the lowest power at the precessional band between 12.7 and 10.9 Ma and the highest power at the precessional band between 10.9 and 9.0 Ma (Figure S8). The $\delta^{18}O$ record additionally exhibits significant variability in the obliquity band between 12.7 and 10.9 Ma and between 7.0 and 5.5 Ma. Cross spectral analysis shows an out-of-phase relationship between planktic and benthic foraminiferal $\delta^{18}O$ at the precessional band, with benthic $\delta^{18}O$ leading planktic $\delta^{18}O$ by ~120°–150° at the 23 and 19 kyr precessional bands (Figure S9). Although the lack of coherence does not allow phase relationship estimation at the 23 kyr precessional band between 12.7 and 10.9 Ma, the phase lag of planktic $\delta^{18}O$ is also 150° at the 19 kyr precessional band. Planktic and benthic foraminiferal $\delta^{18}O$ are in-phase at the 41 kyr obliquity band, with a phase lag of *T. sacculifer* $\delta^{18}O$ at the obliquity band of ~30°–60° (Figure S9).

4. Discussion

4.1. Mixed Layer $\delta^{18}O$ as Proxy for Surface Hydrology and Monsoon Variability

A recent sediment trap study based on stable isotopes estimated a calcification depth of 30–65 m for *T. sacculifer* in the northern SCS (Adejare Ladigbolu et al., 2020), indicating that this species lives in the lower part of the mixed layer. Today, the depth and $\delta^{18}O$ composition of the mixed layer in the northern South China exhibit a strong seasonal signal, which is coupled to the reversal of monsoonal winds and evaporation-precipitation budgets. The relatively low amplitude variability of planktic foraminiferal Mg/Ca derived temperatures (2°C–3°C) in comparison to the high amplitude variability of $\delta^{18}O$ during the Miocene (Holbourn et al., 2010, 2018; Steinke et al., 2010) implies that the $\delta^{18}O$ signal is strongly imprinted by changes in $\delta^{18}O_{seawater}$. The present-day precipitation-evaporation budget in the northern SCS is mainly driven by the monsoonal seasonality of rainfall and river runoff from South China. The modern salinity difference between the monsoonal and pre-monsoonal seasons is ~0.7–1.0 psu at the location of Site 1146 (Yi et al., 2020). This strong seasonality in precipitation/runoff amount is also reflected in the $\delta^{18}O$ of precipitation/runoff within the Pearl River catchment (Ruan et al., 2018). Mean monthly weighted precipitation $\delta^{18}O$ varies between −12‰ and −6‰ during the monsoonal season (May–September) and between −6‰ and 0‰ in the pre-monsoonal season (January–April). The variability in the post-monsoonal season is extremely high with large regional differences between −12‰ and −2‰ (Ruan et al., 2018).

4.2. Hematite/Goethite as Proxy for Chemical Weathering and East Asian Monsoon Intensity

The composition of fine-grained detrital iron and clay minerals transported from land and incorporated into marine sediments reflects weathering and erosion in the source area of the terrigenous discharge and has often been used to reconstruct changes in Asian, African, and South American monsoonal climate (Boulay et al., 2005; Chen et al., 2017; Colin et al., 2014; Gaillardet et al., 1999; Galy & France-Lanord, 1999; Harris

Figure 5. Comparison of East Asian Monsoon proxy records from ODP Site 1146 with atmospheric pCO_2 and SST latitudinal thermal gradients between 17 and 5 Ma. (a) Evolution of SST latitudinal thermal gradients from Herbert et al. (2016); (b) Evolution of atmospheric pCO_2 compiled from sources listed below. Note different *y*-axes with corresponding symbols; (c) Gradient between planktic and benthic foraminiferal $\delta^{13}C$ ($\Delta\delta^{13}C$) as indicator of sequestration efficiency of the biological pump; (d) End-member EM1 (interpreted as aeolian dust) derived from grain size analysis at ODP Site 1146 from Wan et al. (2007); (e) DRS-derived chemical weathering proxy record; dark brown smoothed curve based on Stineman function; (f) Mixed layer $\delta^{18}O$; new data between 12.7 and 9 Ma were integrated with previously published data (Holbourn et al., 2010, 2018); (g) Benthic foraminiferal $\delta^{18}O$ from Holbourn et al. (2005, 2007, 2013, 2018). All 1146 data are plotted on revised age model. Blue arrows indicate main cooling steps. Orange shading indicates intervals of relative global warmth. Blue shading indicates interval of global cooling. Gray shading indicates intense carbonate impoverishment in the deep tropical ocean known as the Carbonate Crash. MCO: Miocene Climatic Optimum; MMCT: middle Miocene Climatic Transition. Sources for pCO_2 reconstructions: (1) alkenone data from ODP Sites 925 and 929 (Stoll et al., 2019); (2) alkenone data from ODP Site 806 (Stoll et al., 2019); (3) alkenone data from Zhang et al. (2013), recalibrated by Stoll et al. (2019); (4) alkenone data from Bolton et al. (2016), recalibrated by Stoll et al. (2019); (5) simulation 6, 50th percentile (Tanner et al., 2020); (6) alkenone data from Badger et al. (2013); (7) Boron isotope data from Badger et al. (2013); (8) Boron isotope data from Greenop et al. (2014); (9) Boron isotope data from Raitzsch et al. (2021); (10) alkenone BAYSPAR SST data from Super et al. (2018).

and Mix, 1999, 2002; Z. Liu et al., 2003, 2007; Thiry, 2000; Tian et al., 2011; Wan et al., 2009, 2012; Zhao et al., 2018). Monsoonal climate systems are characterized by distinctive detrital signals due to the intense erosional power of their highly seasonal rainfall regime. However, these signals represent complex proxies that carry information about weathering in the source area, erosion, and transport mechanisms (Clift et al., 2008, 2014; Giosan et al., 2017; Stallard, 1992).

At Site 1146, where the terrigenous component is dominated by the sediment discharge from the Pearl River, the abundance and ratio of the iron oxide-hydroxide minerals hematite and goethite reflect the hydroclimate of lowland drainage areas (e.g., Clift et al., 2019; Harris & Mix, 1999, 2002). Under humid climate conditions, soil colors change from red to yellowish brown, reflecting the mineralogical transformation of hematite (Fe_2O_3) into goethite (FeOOH) (Schwertmann, 1971). Thus, high hematite/goethite values indicate aridity in the terrigenous source region (Kämpf & Schwertmann, 1983). Due to their very distinct color reflectance spectra, the detection limit for both hematite and goethite with DRS is better than 0.1%, and their ratio has been commonly used as an indicator of aridity/humidity in terrigenous loess-soil sequences and in the catchments of riverine terrigenous sediment discharge (Debret et al., 2011; Harris & Mix, 1999, 2002; Ji et al., 2002, 2004; Zhang et al., 2007).

4.3. Evolution of East Asian Monsoon From ~17 to 5 Ma

4.3.1. Intensification of Seasonal Monsoon Regime During Middle Miocene Climatic Transition

Combined records of planktic foraminiferal $\delta^{18}O$ and hematite/goethite (Figures 5 and S3) suggest that a year-round warm, humid tropical climate prevailed over southeastern Asia during the MCO. Abundant precipitation likely drove intense chemical weathering between ~16 and 14.7 Ma, as shown by the lowest hematite/goethite values within the entire ~17–5 Ma interval. Support for this interpretation is provided by the relatively low mixed layer $\delta^{18}O$ mean values, suggestive of warm and fresh surface waters at Site 1146 and by the strong response of $\delta^{18}O$ to precession, indicating that local insolation forcing mainly controlled the strength of tropical convection and intensity of annual precipitation (Figures 3 and 5). Observations, proxy data, and modeling simulations indicated that the tropical climate zone expands under global warming, driving a shift of the main ocean gyres and subtropical fronts toward higher latitudes and promoting changes in global atmospheric circulation (e.g., Norris et al., 2016; Son et al., 2018; Yang, Lohmann, Krebs-Kanzow, et al., 2020; Yang, Lohmann, Lu, et al., 2020). Globally elevated temperatures, high atmospheric pCO_2, and the markedly reduced latitudinal gradient during the MCO (Figures 5 and S10) would have promoted tropical expansion and attendant displacement of the westerly winds, jet streams, and storm tracks toward higher latitudes.

During the MMCT, stepwise global cooling and expansion of the EAIS would have induced a contraction of the tropics and a shift of climatic zones toward the lower latitudes, leading to a reorganization of atmospheric convective cells and major changes in the intensity and seasonality of precipitation. An overall increase in hematite/goethite coupled to a stepwise increase in mixed layer $\delta^{18}O$ mean values between ~14.7 and 13.8 Ma suggests a long-term decrease in regional precipitation associated with stepwise glacial expansion (Figures 5 and S3). Transient episodes of surface warming and freshening ($\delta^{18}O$ decreases) at high eccentricity between ~14.7 and 13.5 Ma, previously interpreted as northward incursions of the ITCZ in response to Antarctic ice growth and Southern Hemisphere cooling (Holbourn et al., 2010), reveal a highly dynamic hydrological regime during the MMCT. This is also consistent with the strong response of mixed layer $\delta^{18}O$ to precessional insolation forcing during this interval (Figure 3). These results can be explained by a shift from a more equable, warm, and wet climate in a high CO_2 world during the MCO to a more variable monsoonal regime during the MMCT with precipitation concentrated during the summer season. The prevalence of cool and dry conditions during the winter season would have led to a decrease in chemical weathering and to a reduced terrestrial input into the ocean.

4.3.2. Summer Monsoon Decline Linked to Middle to Late Miocene Carbonate Crash?

Substantially higher mean mixed layer $\delta^{18}O$ coupled to a decrease in amplitude variability together with elevated hematite/goethite between ~13.5 and 12.7 Ma signal a shift to a drier climate regime (Figures 4, 5, and S4–S5). From ~12.7 to 10.9 Ma, hematite/goethite displays the highest values within the entire ~17–5 Ma interval, indicating considerable weakening of the summer monsoon and increased aridification

(Figures 4 and 5). The simultaneous increase in the aeolian dust input at Site 1146 (Wan et al., 2007; Figure 5) also implies enhanced aridity in the Asian interior. Furthermore, mixed layer $\delta^{18}O$ exhibits extremely low amplitude variability ($\delta^{18}O$ standard deviation ~0.1‰) and shows little response to precession between ~12.8 and 11.6 Ma (Figure 3), supporting a general decline of the summer monsoon over this period. This transition to substantially more arid conditions may have been linked to an overall decrease in the water content of the atmosphere and attendant changes in moisture budgets following the final step at ~13.1 Ma of middle Miocene Antarctic glaciation and global cooling (Figure 5). From ~11.5 to 10.9 Ma, transient $\delta^{18}O$ decreases as well as enhanced response to precession at eccentricity maxima (Figures 4 and 5), however, point to an intermittent strengthening of the summer monsoon with heightened sensitivity to local insolation forcing.

The ~12.7–10.9 Ma interval, characterized by the driest conditions within the entire middle to late Miocene, also coincided with extended episodes of intense carbonate depletion in the deep ocean that affected all major tropical basins, and are together termed the Carbonate Crash (Dickens & Owen, 1999; Farrell et al., 1995; Lyle et al., 1995; Mayer et al., 1985, 1986). Such a global reduction in the carbonate flux to the deep sea sediment reservoir needs to be compensated either by extensive carbonate deposition on shelves or in epeiric seas, or by a decrease in the flux of calcium and HCO_3^- (alkalinity) to the ocean (Milliman, 1993). However, the major sea-level fall associated with Antarctic ice expansion substantially reduced the surface area of shelves and shallow seas available for carbonate deposition. Global cooling, on the other hand, would have resulted in a contraction of the tropical rain belt, thus, decreasing the HCO_3^- input from monsoonal low-latitude rivers. In addition, aridification in Europe and central Asia between ~13 and 11 Ma (Böhme, 2008; Tang & Ding, 2013) likely reduced the HCO_3^- flux to the ocean further, as midlatitude rivers have a high dissolved inorganic carbon content in relation to their relatively small freshwater discharge (Cai et al., 2008). The gradient between benthic and planktic foraminiferal $\delta^{13}C$ additionally displays a long-term decrease during this interval, indicating weakening of the biological pump (Figures 4 and 5). Thus, data from our study support that a decline of the summer monsoon and attendant decrease in the riverine input of nutrients and alkalinity to the ocean within a global context of cooling and drying contributed to sustain carbonate depletion in the deep ocean between ~12.7 and 10.9 Ma.

4.3.3. Strengthening of Summer Monsoon From ~10.8 to 9 Ma

The interval ~10.8–9 Ma, corresponding to the recovery phase from the Carbonate Crash, is characterized by an intensification of the summer monsoon, as shown by an overall decrease in hematite/goethite and substantially lower mixed layer mean $\delta^{18}O$ values at Site 1146 (Figures 4, 5, and S4). The end of the most intense phase of the Carbonate Crash coincided with an abrupt warming episode, the Tortonian thermal maximum, characterized by a sharp drop of ~1‰ in benthic foraminiferal $\delta^{18}O$ associated with a major $\delta^{13}C$ decrease at ~10.8 Ma. At Site 1146, the marked increase in mixed layer $\delta^{18}O$ during this transient warming is most likely due to early diagenesis at the sea floor, as this interval corresponds to a distinct pyrite-rich, bluish-green layer with calcite (Wang et al., 2000), likely associated with a decline in SCS deep water oxygenation (Holbourn et al., 2013). The color reflectance red-green parameter (a*) within this interval also shows a drastic decrease to green values and magnetic susceptibility decreases from ~40 to ~10 SI units, due to pyrite formation (Holbourn et al., 2013; Wang et al., 2000). This strongly affects the C_{RAT} and hematite/goethite spectral reflectance records, limiting their potential as weathering/erosion proxies (supporting information).

The distinctive warm event at ~10.8 Ma was recently documented in a well-resolved isotope record from Site U1443, drilled on the Ninetyeast Ridge in the Indian Ocean (Lübbers et al., 2019), underpining its supra-regional occurrence. It coincides with an unusual orbital congruence (maxima in 100, 400 kyr eccentricity and maximum in 2.4 Myr amplitude modulation of eccentricity, Figures 4 and 5), and is reminiscent of eccentricity-paced hyperthermal events during the MCO (Holbourn et al., 2013). The benthic foraminiferal $\delta^{18}O$ minimum at ~10.8 Ma occurs within a background of orbitally paced $\delta^{18}O$ and $\delta^{13}C$ variations, demonstrating high sensitivity of the ocean-climate system to eccentricity and obliquity forcing throughout this period. Several of the more muted warming events between ~10.8 and 9 Ma also coincide with changes in sediment color, indicating episodes of decreased bottom water ventilation at ET maxima (Figures 4 and 5). Our results indicate that dynamic changes in tropical hydrology and ocean circulation between ~10.8 and

9 Ma led to a progressive intensification of the summer monsoon and an increased input of alkalinity to the ocean, which were instrumental in the recovery from the Carbonate Crash.

4.3.4. Late Miocene Biogenic Bloom

A rise in benthic and planktic foraminiferal $\delta^{13}C$ after ~9 Ma marks the onset of a prolonged, positive excursion, which consists of four distinct $\delta^{13}C$ cycles paced by 400 kyr long eccentricity and lasts until 7.7 Ma (Figure 3). This prominent positive excursion was originally identified as $\delta^{13}C$ maximum CM7 in low-resolution isotope records from several ocean basins (Woodruff & Savin, 1991). The global occurrence and extended duration of the $\delta^{13}C$ shift imply that it was associated with fundamental changes in the carbon cycle. At Site 1146, the $\delta^{13}C$ excursion coincides with a marked increase in sedimentation rates and in the gradient between benthic and planktic foraminiferal $\delta^{13}C$ (Figures 5 and S6), suggesting enhanced biogenic accumulation and terrigenous input. Coeval increases in carbonate and opal accumulation were previously identified in the eastern equatorial Pacific Ocean and at upwelling locations in the Atlantic and Indian Oceans (e.g., Dickens & Owen, 1999; Diester-Haass et al., 2004; Farrell et al., 1995), and are collectively known as the Biogenic Bloom.

At Site 1146, low mean mixed layer $\delta^{18}O$ together with low hematite/goethite indicate that a strong summer monsoon regime prevailed between ~9 and 7 Ma (Figures 5 and S4). The development of a vigorous convective monsoonal circulation at low latitudes was likely favored by a steeper latitudinal thermal gradient (Figure 5). Relatively high benthic foraminiferal $\delta^{18}O$ between ~9 and 7 Ma also suggests an expanded Antarctic ice sheet and colder Southern Ocean temperatures during this period. Between ~7.7 and 7 Ma, a massive long-term decrease in $\delta^{13}C$ of >1‰, corresponding to the global decline known as the late Miocene carbon isotope shift (LMCIS; Keigwin, 1979; Keigwin & Shackleton, 1980), indicates fundamental changes in carbon cycling during the peak phase of the Biogenic Bloom (Figures 3 and 5). This period was characterized by global cooling (Herbert et al., 2016), a marked decline in atmospheric pCO_2 (Tanner et al., 2020; Figure 5), and by widespread continental aridification of the Northern Hemisphere (e.g., Guo et al., 2002; J. Liu et al., 2016; Wan et al., 2007).

A slight increase in mixed layer $\delta^{18}O$ between ~7.5 and 7 Ma at Site 1146 supports a progressive weakening of the summer monsoon over Southeast Asia during the LMCIS (Figure 5). Between ~7 and 5.5 Ma, cooling was associated with a marked increase in the mean and amplitude variability of planktic $\delta^{18}O$ (Figures 3 and S4–S5), previously interpreted as a decline of the wet summer monsoon and intensification of the dry winter monsoon (Holbourn et al., 2018). Hematite/goethite only registers a slight increase over this period, which may be related to the decreased riverine input of fine-grained sediment from the northwestern mountainous area of the Pearl River catchment due to reduced erosion from the weaker summer monsoon. This would have induced a shift toward sediment originating from the proximal part of the Pearl River, where subtropical vegetation was dominant and goethite more abundant in soils. The grain-size analysis of Wan et al. (2007) reveals a major increase in aeolian dust after ~7 Ma (Figure 5), indicating that intensified dry winter monsoonal winds carried dust from arid regions in the central parts of the East Asian continent toward the location of Site 1146 during this cooler period.

The interval ~7–5.5 Ma was also marked by a long-term trend toward higher benthic foraminiferal $\delta^{18}O$, which culminated in a succession of sharp maxima (TG events) before reversing after 5.5 Ma (Figure 2). These global deep water $\delta^{18}O$ maxima, coincident with planktic $\delta^{18}O$ maxima and temperature decreases of 2°C–3°C at Site 1146, were tentatively attributed to transient Northern Hemisphere glaciations (Holbourn et al., 2018). Furthermore, the gradient between benthic and planktic foraminiferal $\delta^{13}C$ reaches peak values between ~7 and 5.5 Ma, during the most intense phase of the Biogenic Bloom (Figure 5). We speculate that steepening of the latitudinal thermal gradient after ~7 Ma (Herbert et al., 2016; Figure 5) strengthened the Hadley and Walker circulation, helping to drive ocean upwelling and productivity and promoting deep ocean carbon storage and lowering atmospheric pCO_2 in a positive feedback loop. However, these climatic trends abruptly reversed after 5.5 Ma, as shown by a decline in hematite/goethite and by decreases in benthic and planktic foraminiferal $\delta^{18}O$ and $\Delta\delta^{13}C$ (Figure 5).

4.4. Drivers of East Asian Monsoon Evolution

Some recent modeling studies investigating the main controls on the long-term evolution of the Asian Monsoon yielded very different results (e.g., Acosta & Huber, 2020; Farnsworth et al., 2019). A low-resolution experiment extending back to the Early Cretaceous suggested that the East Asian Monsoon was predominantly controlled by gradual uplift of the Himalayan-Tibetan region since the Late Cretaceous (Farnsworth et al., 2019). By contrast, high-resolution climate simulations by Acosta and Huber (2020) indicated that monsoon flow is largely governed by sea surface temperature gradients and that topography mainly redirects onshore flow, which affects the spatial and temporal distribution of precipitation. These contradictory results largely stem from differences in model resolution and prescribed boundary conditions, which strongly influence outputs. A major limitation of low-resolution simulations, for instance, is that they fail to accurately capture monsoon dynamics (Acosta & Huber, 2017, 2020) and are, therefore, not compatible with high-resolution paleoclimate reconstructions.

The orbital-scale variability of the East Asian Monsoon is driven by changes in the strength and spatial extent of atmospheric convective cells in conjunction with the available heat and moisture in the source area (e.g., Caley et al., 2014; Mohtadi et al., 2016, and references therein). However, the relative impact of changing insolation forcing and greenhouse gases on the latitudinal thermal gradient and on the strength and extent of the atmospheric convection has been intensely debated. Particular disagreement exists in estimating the effects of greenhouse gas-driven global warming on the intensity of monsoonal circulation (Birner et al., 2014; Post et al., 2014; Mantsis et al., 2017; Mamalakis et al., 2021). Coupled circulation models predicted that during greenhouse warming, the heat input over Asia prevails on a similar or lower level than in the tropics, the atmospheric circulation remains unchanged or weakens, and the spatial extent and intensity of monsoonal rainfall is highly variable depending on local orography, land-sea distribution, and albedo (Kitoh, 2017; Vecchi & Soden, 2007). In contrast, during Northern Hemisphere precessional insolation warming, the net energy input over the Northern Hemisphere Asian landmass increases, leading to a stronger thermal contrast with the tropics and intensification of monsoons due to strengthening of the atmospheric circulation (D'Agostino et al., 2019). However, a new synthesis of Miocene modeling efforts by Burls et al. (2021) underlined the fundamental role of CO_2 as the main control on long-term Miocene warmth. This synopsis underpins, in particular, the role of atmospheric CO_2 as a primary agent by which changing temperature gradients influenced moisture fluxes and monsoon convection.

At Site 1146, planktic $\delta^{18}O$ exhibits a strong response to precessional insolation forcing, except during the Carbonate Crash, when the summer monsoon weakened (Figure 3). The antiphase relationship of planktic and benthic foraminiferal $\delta^{18}O$ records at the precessional band (Figure S9) implies that deep water $\delta^{18}O$ was mainly driven by Antarctic climate variability, as the Southern Ocean was the main locus of deep water formation during the Miocene; by contrast, mixed layer $\delta^{18}O$ responded to local Northern Hemisphere insolation forcing. The significant obliquity component in both records as well as the high coherence and consistent phase relationship at the obliquity band suggest that the latitudinal temperature gradient exerted additional control on SCS hydrology. This can be explained by obliquity-induced variations on the seasonality of radiation and the interhemispheric insolation gradient, which drive cross-equatorial moisture transfer (e.g., Bosmans et al., 2015; Mantsis et al., 2014). Comparison of long-term changes in the latitudinal thermal gradient and atmospheric pCO_2 with our monsoon proxy data (Figure 5) supports that high-latitude cooling and declining pCO_2 were associated with major variations in the intensity and characteristics of the East Asian Monsoon during the middle to late Miocene.

The Miocene evolution of the East Asian Monsoon at Site 1146 suggests that extended periods of global warming (probably induced by greenhouse gas increases) favored the latitudinal expansion of tropical convection and precipitation, whereas global cooling promoted increased seasonality of monsoonal rainfall in the subtropical Northern Hemisphere. Evidence for abundant precipitation and runoff from ~15.6 to 14.7 Ma during the MCO supports northward expansion of the tropical rain belt in response to greenhouse gas forcing. By contrast, monsoon seasonality increased during the MMCT, as the tropics contracted in concert with Antarctic ice sheet expansion and global cooling. Our results also demonstrate that the long-term evolution of this highly dynamic climate feature through the middle to late Miocene was linked to changes in the global carbon cycle through intricate internal feedback processes involving, atmospheric pCO_2, the

latitudinal thermal gradient, deep ocean, and terrestrial carbon storage as well as atmospheric and oceanic circulation.

5. Conclusions

Data from this study indicate that secular variations in local insolation forcing and in Southern Hemisphere ice volume, influencing the latitudinal thermal gradient, evaporation-moisture budgets, and the strength of the tropical convection, exerted a major control on the evolution of the East Asian Monsoon during the middle to late Miocene stepwise climate cooling. These dynamic changes in tropical hydrology also had important repercussions for global climate evolution. In particular, data from this study support that weakening of the Southeast Asian summer monsoon between ~13 and 10.9 Ma, following global cooling and ice sheet expansion during the MMCT, contributed to the development of the Carbonate Crash by decreasing one of the main inputs of nutrients and alkalinity to the global ocean. Tectonic uplift of the high Himalaya through the middle to late Miocene may, additionally, have played a critical role in driving major climatic transitions such as the MMCT and LMCIS by redirecting monsoon flow and altering large-scale weathering and erosion patterns. Such re-organization would have induced long-term variations in tropical precipitation and productivity that affected the global carbon cycle and atmospheric CO_2 and preconditioned the ocean-climate system for change toward irreversible tipping points. However, detailed integration of Neogene terrestrial and marine records is urgently required to resolve the relative timing of climatic events and Himalayan uplift in order to better understand the tectonic impact on monsoon circulation as well as the intricate feedback processes involved.

Data Availability Statement

This study used samples and data provided by the International Ocean Discovery Program (IODP). All data presented in this study are available from the Data Publisher for Earth & Environmental Science ((PANGAEA.de/; https://doi.pangaea.de/10.1594/PANGAEA.931111).

Acknowledgments
This project was funded by the Deutsche Forschungsgemeinschaft (Grant Ku649/30-1 and 31-1). The authors thank the captain, crew, technical staff, and shipboard scientific party of ODP Leg 184 for their efforts and dedication. The authors thank the editor Sarah Feakins and two anonymous reviewers for constructive critical comments that helped us to improve the manuscript. Open Access funding enabled and organized by Projekt DEAL.

References

Acosta, R. P., & Huber, M. (2017). The neglected Indo-Gangetic Plains low-level jet and its importance for moisture transport and precipitation during the peak summer monsoon. *Geophysical Research Letters*, *44*, 8601–8610. https://doi.org/10.1002/2017GL074440

Acosta, R. P., & Huber, M. (2020). Competing topographic mechanisms for the summer Indo-Asian monsoon. *Geophysical Research Letters*, *47*, e2019GL085112. https://doi.org/10.1029/2019gl085112

Adejare Ladigbolu, I., Li, H., Li, B., Wiesner, M. G., Zhang, J., Sun, L., et al. (2020). Calcification depths and temperatures of planktonic foraminifera off southwest Hainan Island and their paleoceanographic implications. *Marine Micropaleontology*, *158*, 101878. https://doi.org/10.1016/j.marmicro.2020.101878

An, Z., Kutzbach, J. E., Prell, W. L., & Porter, S. C. (2001). Evolution of Asian monsoons and phased uplift of the Himalaya-Tibetan plateau since Late Miocene times. *Nature*, *411*, 62–66.

Badger, M. P. S., Lear, C. H., Pancost, R. D., Foster, G. L., Bailey, T. R., Leng, M. J., & Abels, H. A. (2013). CO_2 drawdown following the middle Miocene expansion of the Antarctic Ice Sheet. *Paleoceanography*, *28*, 42–53. https://doi.org/10.1002/palo.20015

Balsam, W. L., & Damuth, J. E. (2000). Further investigations of shipboard vs shore-based spectral data: Implications for interpreting Leg 164 sediment composition. In C. K. Paull, R. Matsumoto, P. J. Wallace, & W. P. Dillon (Eds.), *Proceedings of the Ocean Drilling Program, Scientific Results* (Vol. 164, pp. 313–324). Ocean Drilling Program.

Balsm, W. L., Damuth, J. E., & Deaton, B. (2007). Marine sediment components: Identification and dispersal assessed by diffuse reflectance spectrophotometry. *International Journal of Environment and Health*, *1/3*, 403–426. https://doi.org/10.1504/ijenvh.2007.017869

Biasutti, M., Voigt, A., Boos, W. R., Braconnot, P., Hargreaves, J. C., Harrison, S. P., et al. (2018). Global energetics and local physics as drivers of past, present and future monsoons. *Nature Geoscience*, *11*, 392–400. https://doi.org/10.1038/s41561-018-0137-1

Birner, T., Sean, M., Davis, S. M., Dian, J., & Seidel, D. J. (2014). The changing width of Earth's tropical belt. *Physics Today*, *67*(12), 38–44. https://doi.org/10.1063/PT.3.2620

Böhme, M., Ilg, A., & Winklhofer, M. (2008). Late Miocene "washhouse" climate in Europe. *Earth and Planetary Science Letters*, *275*(3–4), 393–401. https://doi.org/10.1016/j.epsl.2008.09.011

Bolton, C. T., Hernandez-Sanchez, M. T., Fuertes, M.-A., Gonzalez-Lemos, S., Abrevaya, L., Mendez-Vicente, A., et al. (2016). Decrease in coccolithophore calcification and CO_2 since the middle Miocene. *Nature Communications*, *7*. https://doi.org/10.1038/ncomms10284

Boos, W. R., & Kuang, Z. (2010). Dominant control of the South Asian monsoon by orographic insulation versus plateau heating. *Nature*, *463*, 218–222. https://doi.org/10.1038/nature08707

Bosmans, J. H. C., Hilgen, F. J., Tuenter, E., & Lourens, L. J. (2015). Obliquity forcing of low-latitude climate. *Climate of the Past*, *11*(10), 1335–1346. https://doi.org/10.5194/cp-11-1335-2015

Boulay, S., Colin, C., Trentesaux, A., Frank, N., & Liu, Z. F. (2005). Sediment sources and East Asian monsoon intensity over the last 450 kyr: Mineralogical and geochemical investigations on South China Sea sediment. *Palaeogeography, Palaeoclimatology, Palaeoecology*, *228*, 260–277. https://doi.org/10.1016/j.palaeo.2005.06.005

Burls, N. J., Bradshaw, C. D., De Boer, A. M., Herold, N., Huber, M., Pound, M., et al. (2021). Simulating Miocene warmth: Insights from an opportunistic Multi-Model ensemble (MioMIP1). *Paleoceanography and Paleoclimatology*, *36*. https://doi.org/10.1029/2020PA004054

Cai, W.-J., Guo, X., Chen, C.-T. A., Dai, M., Zhang, L., Zhai, W., et al. (2008). A comparative overview of weathering intensity and HCO_3- flux in the world's major rivers with emphasis on the Changjiang, Huanghe, Zhujiang (Pearl) and Mississippi Rivers. *Continental Shelf Research*, *28*, 1538–1549. https://doi.org/10.1016/j.csr.2007.10.014

Caley, T., Roche, D. M., & Renssen, H. (2014). Orbital Asian summer monsoon dynamics revealed using an isotope-enabled global climate model. *Nature Communications*, *5*, 6–11. https://doi.org/10.1038/ncomms6371

Chen, Q., Liu, Z. F., & Kissel, C. (2017). Clay mineralogical and geochemical proxies of the East Asian summer monsoon evolution in the South China Sea during Late Quaternary. *Scientific Reports*, *7*, 42083. https://doi.org/10.1038/srep42083

Clift, P. D., Hodges, K., Heslop, D., Hannigan, R., Hoang, L. V., & Calves, G. (2008). Greater Himalayan exhumation triggered by Early Miocene monsoon intensification. *Nature Geoscience*, *1*, 875–880. https://doi.org/10.1038/ngeo351

Clift, P. D., Kulhanek, D. K., Zhou, P., Bowen, M. G., Vincent, S. M., Lyle, M., & Hahn, A. (2019). Chemical weathering and erosion responses to changing monsoon climate in the Late Miocene of Southwest Asia. *Geological Magazine*, *157*, 939–955. https://doi.org/10.1017/S0016756819000608

Clift, P. D., Wan, S., & Blusztajn, J. (2014). Reconstructing chemical weathering, physical erosion and monsoon intensity since 25 Ma in the northern South China Sea: A review of competing proxies. *Earth-Science Reviews*, *130*, 86–102. https://doi.org/10.1016/j.earscirev.2014.01.002

Colin, C., Siani, G., Liu, Z., Blamart, D., Skonieczny, C., Zhao, Y., et al. (2014). Late Miocene to early Pliocene climate variability off NW Africa (ODP Site 659). *Palaeogeography, Palaeoclimatology, Palaeoecology*, *401*, 81–95. https://doi.org/10.1016/j.palaeo.2014.02.015

D'Agostino, R., Lionello, P., Adam, O., & Schneider, T. (2019). Factors controlling Hadley circulation changes from the last glacial maximum to the end of the 21st century. *Geophysical Research Letters*, *44*, 8585–8591.

Deaton, B. C., & Balsam, W. L. (1991). Visible spectroscopy—A rapid method for determining hematite and goethite concentration in geological materials. *Journal of Sedimentary Geology*, *61*(4), 628–632. https://doi.org/10.1306/d4267794-2b26-11d7-8648000102c1865d

Debret, M., Sebag, D., Desmet, M., Balsam, W., Copard, Y., Mourier, B., et al. (2011). Spectrocolorimetric interpretation of sedimentary dynamics: The new "Q7/4 diagram". *Earth-Science Reviews*, *109*(1–2), 1–19. https://doi.org/10.1016/j.earscirev.2011.07.002

De Vleeschouwer, D., Drury, A. J., Vahlenkamp, M., Rochholz, F., Liebrand, D., & Pälike, H. (2020). High-latitude biomes and rock weathering mediate climate–carbon cycle feedbacks on eccentricity timescales. *Nature Communications*, *11*, 5013.2020. https://doi.org/10.1038/s41467-020-18733-w

Dickens, G. R., & Owen, R. M. (1999). The latest Miocene–early Pliocene biogenic bloom: A revised Indian Ocean perspective. *Marine Geology*, *161*(1), 75–91. https://doi.org/10.1016/S0025-3227(99)00057-2

Diester-Haass, L., Meyers, P. A., & Bickert, T. (2004). Carbonate crash and biogenic bloom in the late Miocene: Evidence from ODP Sites 1085, 1086, and 1087 in the Cape Basin, southeast Atlantic Ocean. *Paleoceanography*, *19*, PA1007. https://doi.org/10.1029/2003pa000933

Ding, L., Spicer, R. A., Yang, J., Xu, Q., Cai, F., Li, S., et al. (2017). Quantifying the rise of the Himalaya orogen and implications for the South Asian monsoon. *Geology*, *45*, 215–218. https://doi.org/10.1130/g38583.1

Farnsworth, A. J., Lunt, D. J., Robinson, S. A., Valdes, P. J., Roberts, W., Clift, P. D., et al. (2019). Past East Asian monsoon evolution controlled by paleogeography, not CO_2. *Science Advances*, *5*(10), eaax1697. https://doi.org/10.1126/sciadv.aax1697

Farrell, J. W., Raffi, I., Janecek, T. R., Murray, D. W., Levitan, M., Dadey, K. A., et al. (1995). Late Neogene sedimentation patterns in the eastern equatorial Pacific. In N. G. Pisias, L. A. Mayer, T. R. Janecek, A. Palmer-Julson, & T. H. van Andel (Eds.), *Proceedings of the Ocean Drilling Program, Scientific Results* (Vol. 138, pp. 717–756). Ocean Drilling Program. https://doi.org/10.2973/odp.proc.sr.138.143.1995

Gaillardet, J., Dupre, B., Louvat, P., & Allègre, C. J. (1999). Global silicate weathering and CO_2 consumption rates deduced from the chemistry of large rivers. *Chemical Geology*, *159*, 3–30. https://doi.org/10.1016/s0009-2541(99)00031-5

Galy, A., & France-Lanord, C. (1999). Weathering processes in the Ganges-Brahmaputra basin and the riverine alkalinity budget. *Chemical Geology*, *159*, 31–60. https://doi.org/10.1016/s0009-2541(99)00033-9

Giosan, L., Flood, R. D., & Aller, R. C. (2002). Paleoceanographic significance of sediment color on western North Atlantic drifts: I. Origin of color. *Marine Geology*, *189*, 25–41. https://doi.org/10.1016/s0025-3227(02)00321-3

Giosan, L., Ponton, C., Usman, M., Blusztajn, J., Fuller, D. Q., Galy, V., et al. (2017). Short communication: Massive erosion in monsoonal central India linked to late Holocene land cover degradation. *Earth Surface Dynamics*, *5*, 781–789. https://doi.org/10.5194/esurf-5-781-2017

Greenop, R., Sosdian, S. M., Henehan, M. J., Wilson, P. A., Lear, C. H., & Foster, G. L. (2014). Orbital forcing, ice volume, and CO_2 across the Oligocene-Miocene transition. *Paleoceanography and Paleoclimatology*, *34*, 316–328. https://doi.org/10.1029/2018PA003420

Guo, Z. T., Ruddiman, W. F., Hao, Q. Z., Wu, H. B., Qiao, Y. S., Zhu, R. X., et al. (2002). Onset of Asian desertification by 22 Myr ago inferred from loess deposits in China. *Nature*, *416*, 159–163.

Hain, M. P., Sigman, D. M., & Haug, G. H. (2014). The biological pump in the past *Treatise on geochemistry (second edition). Volume 8: The oceans and marine geochemistry* (pp. 485–517). Elsevier. https://doi.org/10.1016/B978-0-08-095975-7.00618-5

Hall, R. (1998). The plate tectonics of Cenozoic SE Asia and the distribution of land and sea. In R. Hall, & J. D. Holloway (Eds.), *Biogeography and geological evolution of SE Asia* (pp. 99–131). Backhuys Publishers.

Hammer, Ø., Harper, D. A. T., & Ryan, P. D. (2001). PAST: Paleontological statistics software package for education and data analysis. *Palaeontologia Electronica*, *4*(1), 9.

Harris, S. E., & Mix, A. C. (1999). Pleistocene precipitation balance in the Amazon Basin recorded in deep sea sediments. *Quaternary Research*, *51*, 14–26. https://doi.org/10.1006/qres.1998.2008

Harris, S. E., & Mix, A. C. (2002). Climate and tectonic influences on continental erosion of tropical South America, 0–13 Ma. *Geology*, *30*, 447–450. https://doi.org/10.1130/0091-7613(2002)030<0447:catioc>2.0.co;2

Herbert, T. D., Lawrence, K. T., Tzanova, A., Peterson, L. C., Caballero-Gill, R., & Kelly, C. S. (2016). Late Miocene global cooling and the rise of modern ecosystems. *Nature Geoscience*, *9*, 843–847. https://doi.org/10.1038/ngeo2813

Heslop, D., von Dobeneck, T., & Höcker, M. (2007). Using non-negative matrix factorization in the "unmixing" of diffuse reflectance spectra. *Marine Geology*, *241*, 63–78. https://doi.org/10.1016/j.margeo.2007.03.004

Holbourn, A. E., Kuhnt, W., Clemens, S., Kochhann, K., Jöhnck, J., Lübbers, J., & Andersen, N. (2018). Late Miocene climate cooling and intensification of southeast Asian winter monsoon. *Nature Communication*, *9*, 1584. https://doi.org/10.1038/s41467-018-03950-1

Holbourn, A. E., Kuhnt, W., Clemens, S., Prell, W., & Andersen, N. (2013). Middle to late Miocene stepwise climate cooling: Evidence from a high-resolution deep water isotope curve spanning 8 million years. *Paleoceanography*, *28*, 688–699. https://doi.org/10.1002/2013pa002538

Holbourn, A. E., Kuhnt, W., Kochhann, K. G. D., Andersen, N., & Meier, K. J. S. (2015). Global perturbation of the carbon cycle at the onset of the Miocene climatic optimum. *Geology*, *43*, 123–126. https://doi.org/10.1130/G36317.1

Holbourn, A. E., Kuhnt, W., Kochhann, K., Matsuzaki, K. M., & Andersen, N. (2020). Middle Miocene climate-carbon cycle dynamics: A key to understand future trends on a warmer Earth? *PANGAEA*. https://doi.org/10.1130/G34890.1
Holbourn, A. E., Kuhnt, W., Lyle, M., Schneider, L., Romero, O., & Andersen, N. (2014). Middle Miocene climate cooling linked to intensification of eastern equatorial Pacific upwelling. *Geology*, *42*, 19–22. https://doi.org/10.1130/G34890.1
Holbourn, A. E., Kuhnt, W., Regenberg, M., Schulz, M., Mix, A., & Andersen, N. (2010). Does Antarctic glaciation force migration of the tropical rain belt? *Geology*, *38*, 783–786. https://doi.org/10.1130/G31043.1
Holbourn, A. E., Kuhnt, W., Schulz, M., & Erlenkeuser, H. (2005). Impacts of orbital forcing and atmospheric carbon dioxide on Miocene ice-sheet expansion. *Nature*, *438*, 483–487. https://doi.org/10.1038/nature04123
Holbourn, A. E., Kuhnt, W., Schulz, M., Flores, J.-A., & Andersen, N. (2007). Orbitally-paced climate evolution during the middle Miocene "Monterey" carbon isotope excursion. *Earth and Planetary Science Letters*, *261*, 534–550. https://doi.org/10.1016/j.epsl.2007.07.026
Ji, J. F., Balsam, W., Chen, J., & Liu, L. W. (2002). Rapid and quantitative measurement of hematite and goethite in the Chinese loesspalesosol sequence by diffuse reflectance spectroscopy. *Clays and Clay Minerals*, *50*, 208–216. https://doi.org/10.1346/000986002760832801
Ji, J. F., Chen, J., Balsam, W., Lu, H. Y., Sun, Y. B., & Xu, H. F. (2004). High resolution hematite/goethite records from Chinese loess sequences for the last glacial–interglacial cycle: Rapid climatic response of the East Asian monsoon to the tropical Pacific. *Geophysical Research Letters*, *31*. https://doi.org/10.1029/2003GL018975
Kämpf, N., & Schwertmann, U. (1983). Goethite and hematite in a climosequence in southern Brazil and their application in classification of kaolinitic soils. *Geoderma*, *29*, 27–39. https://doi.org/10.1016/0016-7061(83)90028-9
Kapp, P., & DeCelles, P. G. (2019). Mesozoic-Cenozoic geological evolution of the Himalayan-Tibetan orogen and working tectonic hypothesis. *American Journal of Science*, *319*, 159–254. https://doi.org/10.2475/03.2019.01
Keigwin, L. D. (1979). Late Cenozoic stable isotope stratigraphy and paleoceanography of DSDP Sites from the east equatorial and central north Pacific Ocean. *Earth and Planetary Science Letters*, *45*, 361–382. https://doi.org/10.1016/0012-821x(79)90137-7
Keigwin, L. D., & Shackleton, N. J. (1980). Uppermost Miocene carbon isotope stratigraphy of a piston core in the equatorial Pacific. *Nature*, *284*, 613–614. https://doi.org/10.1038/284613a0
Kitoh, A. (2017). The Asian monsoon and its future change in climate models: A review. *Journal of the Meteorological Society of Japan*, *95*(1), 7–33. https://doi.org/10.2151/jmsj.2017-002
Kochhann, K. G. D., Holbourn, A. E., Kuhnt, W., Channell, J. E. T., Lyle, M., Shackford, J. K., et al. (2016). Eccentricity pacing of eastern equatorial Pacific carbonate dissolution cycles during the Miocene Climatic Optimum. *Paleoceanography*, *31*, 1176–1192. https://doi.org/10.1002/2016PA002988
Kutzbach, J. E., Guetter, P. J., Ruddiman, W. F., & Prell, W. L. (1989). Sensitivity of climate to late Cenozoic uplift in southern Asia and the American west: Numerical experiments. *Journal of Geophysical Research*, *94*(D15), 18393. https://doi.org/10.1029/JD094iD15p18393
Laskar, J., Robutel, P., Joutel, F., Gastineau, M., Correria, A. C. M., & Levrard, B. (2004). A long-term numerical solution for the insolation quantities of the Earth. *Astronomy and Astrophysics*, *428*, 261–285. https://doi.org/10.1051/0004-6361:20041335
Liu, J., Li, J. J., Song, C. H., Yu, H., Peng, T. J., Hui, Z. C., & Ye, X. Y. (2016). Palynological evidence for late Miocene stepwise aridification on the northeastern Tibetan Plateau. *Climate of the Past*, *12*, 1473–1484. https://doi.org/10.5194/cp-12-1473-2016
Liu, Z., Colin, C., Huang, W., Le, K. P., Tong, S., Chen, Z., & Trentesaux, A. (2007). Climatic and tectonic controls on weathering in south China and Indochina Peninsula: Clay mineralogical and geochemical investigations from the Pearl, Red, and Mekong drainage basins. *Geochemistry, Geophysics, Geosystems*, *8*, Q05005. https://doi.org/10.1029/2006GC001490
Liu, Z., Trentesaux, A., Clemens, S. C., Colin, C., Wang, P. X., Huang, B. Q., & Boulay, S. (2003). Clay mineral assemblages in the northern South China Sea: Implications for East Asian monsoon evolution over the past 2 million years. *Marine Geology*, *201*, 133–146. https://doi.org/10.1016/S0025-3227(03)00213-5
Lübbers, J., Kuhnt, W., Holbourn, A. E., Bolton, C. T., Gray, E., Usui, Y., et al. (2019). The middle to late Miocene "carbonate crash" in the equatorial Indian Ocean. *Paleoceanography and Paleoclimatology*, *34*(5), 813–832. https://doi.org/10.1029/2018PA003482
Lyle, M., Dadey, K. A., & Farrell, J. W. (1995). The late Miocene (11–8 Ma) eastern Pacific carbonate crash: Evidence for reorganization of deep-water circulation by the closure of the Panama gateway. In N. G. Pisias, L. A. Mayer, T. R. Janecek, A. Palmer-Julson, & T. H. van Andel (Eds.), *Proceedings of the Ocean Drilling Program* (Vol. 138, pp. 821–838). Ocean Drilling Program. https://doi.org/10.2973/odp.proc.sr.138.157.1995
Mamalakis, A., Randerson, J. T., Yu, J. Y., Pritchard, M. S., Magnusdottir, G., Smyth, P., et al. (2021). Zonally contrasting shifts of the tropical rain belt in response to climate change. *Nature Climate Change*, *11*, 143–151. https://doi.org/10.1038/s41558-020-00963-x
Mantsis, D. F., Lintner, B. R., Broccoli, A. J., Erb, M. P., Clement, A. C., & Park, H. S. (2014). The response of large-scale circulation to obliquity-induced changes in meridional heating gradients. *Journal of Climate*, *27*(14), 5504–5516. https://doi.org/10.1175/JCLI-D-13-00526.1
Mantsis, D. F., Sherwood, S., Allen, R., & Shi, L. (2017). Natural variations of tropical width and recent trends. *Geophysical Research Letters*, *44*, 3825–3832. https://doi.org/10.1002/2016GL072097
Mayer, L. A., Shipley, T. H., & Winterer, E. L. (1986). Equatorial Pacific seismic reflectors as indicators of global oceanographic events. *Science*, *233*(4765), 761–764. https://doi.org/10.1126/science.233.4765.761
Mayer, L. A., Theyer, F., Barron, J. A., Dunn, D. A., Handyside, T., Hills, S., et al. (1985). *Initial reports of the deep sea drilling project* (Vol. 85, p. 1021). U.S. Government Printing. https://doi.org/10.2973/dsdp.proc.85.1985
Milliman, J. D. (1993). Production and accumulation of calcium carbonate in the ocean: Budget of a nonsteady state. *Global Biogeochemical Cycles*, *7*(4), 927–957. https://doi.org/10.1029/93GB02524
Mohtadi, M., Prange, M., & Steinke, S. (2016). Palaeoclimatic insights into forcing and response of monsoon rainfall. *Nature*, *533*(7602), 191–199. https://doi.org/10.1038/nature17450
Norris, J. R., Allen, R. J., Evan, A. T., Zelinka, M. D., O'Dell, C. W., & Klein, S. A. (2016). Evidence for climate change in the satellite cloud record. *Nature*, *536*(7614), 72–75. https://doi.org/10.1038/nature18273
Paillard, D., Labeyrie, L., & Yiou, P. (1996). Macintosh Program performs time-series analysis. *Eos, Transactions American Geophysical Union*, *77*(39), 379. https://doi.org/10.1029/96EO00259
Post, D. A., Timbal, B., Chiew, F. H. S., Hendon, H. H., Nguyen, H., & Moran, R. (2014). Decrease in southeastern Australian water availability linked to ongoing Hadley cell expansion. *Earth's Future*, *2*, 231–238. https://doi.org/10.1002/2013EF000194
Raitzsch, M., Bijma, J., Bickert, T., Schulz, M., Holbourn, A. E., & Kučera, M. (2021). Atmospheric carbon dioxide variations across the middle Miocene climate transition (2021). *Climate of the Past*, *17*, 703–719. https://doi.org/10.5194/cp-17-703-2021
Raymo, M. E., & Ruddiman, W. F. (1992). Tectonic forcing of late Cenozoic climate. *Nature*, *359*, 117–122. https://doi.org/10.1038/359117a0
Ruan, Y., Liu, Z., Yao, Z., & Wang, R. (2018). Temporal and spatial variations of precipitation ^{18}O and controlling factors on the Pearl River Basin and adjacent regions. *Advances in Meteorology*, *2018*, 1–15. https://doi.org/10.1155/2018/1419326

Ryan, W. B. F., Carbotte, S. M., Coplan, J. O., O'Hara, S., Melkonian, A., Arko, R., et al. (2009). Global multi-resolution topography synthesis. *Geochemistry, Geophysics, Geosystems*, *10*, Q03014. https://doi.org/10.1029/2008GC002332

Schulz, M., & Mudelsee, M. (2002). REDFIT: Estimating red-noise spectra directly from unevenly spaced paleoclimatic time series. *Computers & Geosciences*, *28*(3), 421–426. https://doi.org/10.1016/S0098-3004(01)00044-9

Schwertmann, U. (1971). Transformation of hematite to goethite in soils. *Nature*, *232*, 624–625. https://doi.org/10.1038/232624a0

Shackleton, N. J., & Hall, M. A. (1997). The late Miocene stable isotope record, Site 926. In N. J. Shackleton, W. B. Curry, C. Richter, & T. J. Bralower (Eds.), *Proceedings of the Ocean Drilling Program, Scientific Results* (Vol. 154, pp. 367–373). Texas A & M University, Ocean Drilling Program.

Shackleton, N. J., Hall, M. A., & Pate, D. (1995). Pliocene stable isotope stratigraphy of Site 846. In N. G. Pisias, L. A. Mayer, T. R. Janecek, A. Palmer-Julson, & T. H. van Andel (Eds.), *Proceedings of the Ocean Drilling Program, Scientific Results* (Vol. 138, pp. 337–355). Texas A & M University, Ocean Drilling Program. https://doi.org/10.2973/odp.proc.sr.138.117.1995

Son, S. W., Kim, S. Y., & Min, S. K. (2018). Widening of the Hadley cell from Last Glacial Maximum to future climate. *Journal of Climate*, *31*(1), 267–281. https://doi.org/10.1175/jcli-d-17-0328.1

Spicer, R. A., Su, T., Valdes, P. J., Farnsworth, A., Wu, F.-X., Shi, G., et al. (2020). Why the 'Uplift of the Tibetan Plateau' is a myth. *National Science Review*. *8*(1), nwaa091. https://org/10.1093/nsr/nwaa091

Spicer, R. A., Yang, J., Herman, A. B., Kodrul, T., Aleksandrova, G., Maslova, N., et al. (2017). Paleogene monsoons across India and South China: Drivers of biotic change. *Gondwana Research*, *49*, 350–363. https://doi.org/10.1016/j.gr.2017.06.006

Stallard, R. F. (1992). Tectonic processes, continental freeboard, and the rate-controlling step for continental denudation. In G. V. Wolfe (Ed.), *Global biogeochemical cycles* (pp. 93–121). Academic Press. https://doi.org/10.1016/s0074-6142(08)62689-3

Steinke, S., Groeneveld, J., Johnstone, H., & Rendle-Bühring, R. (2010). East Asian summer monsoon weakening after 7.5 Ma: Evidence from combined planktonic foraminifera Mg/Ca and $\delta^{18}O$ (ODP Site 1146; northern South China Sea). *Palaeogeography, Palaeoclimatology, Palaeoecology*, *289*, 33–43. https://doi.org/10.1016/j.palaeo.2010.02.007

Stoll, H. A., Guitian, J., Hernandez-Almeida, I., Mejia, L. M., Phelps, S., Polissar, P., et al. (2019). Upregulation of phytoplankton carbon concentrating mechanisms during low CO_2 glacial periods and implications for the phytoplankton pCO_2 proxy. *Quaternary Science Reviews*, *208*, 1–20. https://doi.org/10.1016/j.quascirev.2019.01.012

Super, J. R., Thomas, E., Pagani, M., Huber, M., O'Brien, C., & Hull, P. M. (2018). North Atlantic temperature and pCO_2 coupling in the early-middle Miocene. *Geology*, *46*(6), 519–522. https://doi.org/10.1130/g40228.1

Tang, Z.-H., & Ding, Z.-L. (2013). A palynological insight into the Miocene aridification in the Eurasian interior. *Palaeoworld*, *22*, 77–85. https://doi.org/10.1016/j.palwor.2013.05.001

Tanner, T., Hernández-Almeida, I., Drury, A. J., Guitián, J., & Stoll, H. (2020). Decreasing atmospheric CO_2 during the late Miocene cooling. *Paleoceanography and Paleoclimatology*, *35*, e2020PA003925. https://doi.org/10.1029/2020PA003925

Thiry, M. (2000). Palaeoclimatic interpretation of clay minerals in marine deposits: An outlook from the continental origin. *Earth-Science Reviews*, *49*, 201–221. https://doi.org/10.1016/s0012-8252(99)00054-9

Tian, J., Xie, X., Ma, W., Jin, H., & Wang, P. (2011). X-ray fluorescence core scanning records of chemical weathering and monsoon evolution over the past 5 Myr in the southern South China Sea. *Paleoceanography*, *26*, PA4202. https://doi.org/10.1029/2010PA002045

Torrence, C., & Compo, G. P. (1998). A practical guide to wavelet analysis. *Bulletin of the American Meteorological Society*, *79*(1), 61–78. https://doi.org/10.1175/1520-0477(1998)079<0061:APGTWA>2.0.CO;2

Vecchi, G. A., & Soden, B. J. (2007). Global warming and the weakening of the tropical circulation. *Journal of Climate*, *20*, 4316–4340. https://doi.org/10.1175/JCLI4258.1

Vincent, E., & Berger, W. H. (1985). Carbon dioxide and polar cooling in the Miocene: The Monterey hypothesis. In W. S. Broecker, & E. T. Sundquist (Eds.), *The carbon cycle and atmospheric CO_2: Natural variations Archean to present. Geophysical Monograph Series* (Vol.32, pp. 455–468). American Geophysical Union.

Wan, S., Clift, P. D., Li, A., Yu, Z., Li, T., & Hu, D. (2012). Tectonic and climatic controls on long-term silicate weathering in Asia since 5 Ma. *Geophysical Research Letters*, *39*, L15611. https://doi.org/10.1029/2012GL052377

Wan, S., Kürschner, W. M., Clift, P. D., Li, A., & Li, T. (2009). Extreme weathering/erosion during the Miocene Climatic Optimum: Evidence from sediment record in the South China Sea. *Geophysical Research Letters*, *36*, L19706. https://doi.org/10.1029/2009GL040279

Wan, S., Li, A., Clift, P. D., & Stuut, J.-B. W. (2007). Development of the East Asian monsoon: Mineralogical and sedimentologic records in the northern South China Sea since 20 Ma. *Palaeogeography, Palaeoclimatology, Palaeoecology*, *254*(3–4), 561–582. https://doi.org/10.1016/j.palaeo.2007.07.009

Wang, P., Prell, W. L., Higginson, M. J., Jain, Z., Kuhnt, W., & Blum, P., et al. (2000). *Proceedings of the Ocean Drilling Program. Initial Reports 184*. 184, 1143–1148. Ocean Drilling Program, Texas A&M University.

Westerhold, T., Marwan, N., Drury, A. J., Liebrand, D., Agnini, C., Anagnostou, E., et al. (2020). An astronomically dated record of Earth's climate and its predictability over the last 66 million years. *Science*, *369*(6509), 1383–1387. https://doi.org/10.1126/science.aba6853

Woodruff, F., & Savin, S. (1991). Mid-Miocene isotope stratigraphy in the deep sea: High-resolution correlations, paleoclimatic cycles, and sediment preservation. *Paleoceanography*, *6*, 755–806. https://doi.org/10.1029/91PA02561

Yang, H., Lohmann, G., Krebs-Kanzow, U., Ionita, M., Shi, X., Sidorenko, D., et al. (2020). Poleward shift of the major ocean gyres detected in a warming climate. *Geophysical Research Letters*, *47*, e2019GL085868. https://doi.org/10.1029/2019GL085868

Yang, H., Lohmann, G., Lu, J., Gowan, E. J., Shi, X., Liu, J., & Wang, Q. (2020). Tropical expansion driven by poleward advancing midlatitude meridional temperature gradients. *Journal of Geophysical Research: Atmospheres*, *125*, e2020JD033158. https://doi.org/10.1029/2020JD033158

Yi, D. L., Melnichenko, O., Hacker, P., & Potemra, J. (2020). Remote sensing of sea surface salinity variability in the South China Sea. *Journal of Geophysical Research: Oceans*, *125*, e2020JC016827. https://doi.org/10.1029/2020JC016827

Zhang, Y. G., Ji, J., Balsam, W. L., Liu, L., & Chen, J. (2007). High resolution hematite and goethite records from ODP 1143, South China Sea: Co-evolution of monsoonal precipitation and El Niño over the past 600,000 years. *Earth and Planetary Science Letters*, *264*, 136–150. https://doi.org/10.1016/j.epsl.2007.09.022

Zhang, Y. G., Pagani, M., Liu, Z., Bohaty, S. M., & DeConto, R. (2013). A 40-million-year history of atmospheric CO_2. *Philosophical Transactions of the Royal Society A*, *371*, 20130096. https://doi.org/10.1098/rsta.2013.0096

Zhao, S., Liu, Z., Colin, C., Zhao, Y., Wang, X., & Jian, Z. (2018). Responses of the East Asian summer monsoon in the low-latitude South China Sea to high-latitude millennial-scale climatic changes during the last glaciation: Evidence from a high-resolution clay mineralogical record. *Paleoceanography and Paleoclimatology*, *33*, 745–765. https://doi.org/10.1029/2017PA003235